Chapter 1
Historical Developments and Future Perspectives in Nuclear Resonance Scattering

Rudolf Rüffer and Aleksandr I. Chumakov

Abstract In few decades, Nuclear Resonance Scattering of synchrotron radiation developed from a dream to an advanced suite of powerful methods, gathering a wide range of applications from general relativity to nanoscience, combining unprecedented properties of nuclear resonance and synchrotron light, and expanding studies to multiply extreme conditions. This article reviews fundamentals of nuclear resonance physics and properties of synchrotron radiation, provides a short historical overview of the fascinating development, major techniques and instrumentation of the method, and gives a brief snapshot of modern applications and yet coming opportunities.

List of Acronyms

ADC	Analog-to-Digital Converter
APD	Avalanche Photo Diode
APS	Advanced Photon Source
BLS	Brillouin Light Scattering
CFD	Constant Fraction Discriminator
CONUSS	COherent NUclear resonant Scattering by Single crystals
CRL	Compound Refracrive Lens
CZ	Cloudy Zone
DAC	Diamond Anvil Cell
DESY	Deutsches ElektronenSYnchrotron
DFT	Density Functional Theory
DORIS	Doppel-Ring-Speicher
DOS	(phonon) Density Of States

R. Rüffer (✉) · A. I. Chumakov
ESRF, 38043 Grenoble, France
e-mail: rueffer@esrf.fr

A. I. Chumakov
e-mail: chumakov@esrf.fr

© Springer Nature Singapore Pte Ltd. 2021

Y. Yoshida and G. Langouche (eds.), *Modern Mössbauer Spectroscopy*,
Topics in Applied Physics 137, https://doi.org/10.1007/978-981-15-9422-9_1

EBS	Extremely Brilliant Source
ESRF	European Synchrotron Radiation Facility
FZP	Fresnel Zone Plates
GGG	Gadolinium Gallium Garnet
GINRS	Grazing Incidence Nuclear Resonance Scattering
HASYLAB	HAmburger SYnchrotronstrahlungsLABor
HRM	High Resolution Monochromator
INS	Inelastic Neutron Scattering
IR	Infra-Red (spectroscopy)
IUVS	Inelastic UltraViolet Scattering
IXS	Inelastic X-ray Scattering
IXSNRA	Inelastic X-ray Scattering with Nuclear Resonance Analysis
KB	Kirkpatrick-Baez
MB	Mössbauer
MCA	Multi-Channel Analyzer
ML	Monolayer
MOKE	Magnetic Optical Kerr Effect
NBD	Nuclear Bragg Diffraction
NCD	Nano-Crystalline Diamond
NFS	Nuclear Forward Scattering
NIS	Nuclear Inelastic Scattering
NQES	Nuclear Quasi-Elastic Scattering
NRS	Nuclear Resonance Scattering
NSAS	Nuclear Small Angle Scattering
PETRA III	Positron Electron Tandem Ring Accelerator
QCP	Quantum Critical Point
RAMAN	RAMAN spectroscopy
RSMR	Rayleigh Scattering of Mössbauer Radiation
SMS	Synchrotron Mössbauer Source
SPring-8	Super Photon Ring 8 GeV
SQUID	Superconducting Quantum Interference Device
SR	Synchrotron Radiation
SRMS	Synchrotron Radiation Mössbauer Spectroscopy
SRPAC	Synchrotron Radiation based Perturbed Angular Correlation
TAC	Time-to-Amplitude Converter
TDI	Time Domain Interferometry
TDPAC	Time Differential Perturbed Angular Correlation
UHRIXS	Ultra-High-Resolution Inelastic X-ray Scattering
UHV	Ultra High Vacuum
XFEL	X-ray Free Electron Laser
XRD	X-Ray Diffraction
YIG	Yttrium Iron Garnet

1.1 Introduction

"Nuclear resonance fluorescence of γ-radiation" without recoil was discovered and explained by R. L. Mößbauer in 1958 ("Kernresonanzfluoreszenz von Gammastrahlung in Ir^{191}" [1, 2]) and later named "Mössbauer effect" and the related spectroscopy consequently Mössbauer spectroscopy. Already shortly after this earth-breaking discovery thoughts went from absorption to scattering and diffraction experiments. Scattering experiments were reported by Black and Moon early as 1960 [3], followed by grazing incidence experiments by Bernstein and Campbell [4], and diffraction experiments by Black et al. [5]. New phenomena such as interference between electronic and nuclear scattering, enhancement of the radiative channel (speed-up), and suppression of the incoherent channels were discovered and clarified. This early period has been reviewed by Smirnov (experiments) [6], and by van Bürck (theory) [7]. At that time synchrotron radiation has already been known since 1947, however, mainly as a nuisance for high energy accelerator experiments.

In the remaining part of the chapter, nuclear resonance and synchrotron radiation will be introduced. The following historical chapter shall in general highlight, on the example of nuclear resonance scattering, the challenges in scientific developments, which are not only scientificly but also technically and politically driven.

The main part is devoted to an overview of the richness of nuclear resonance techniques and spectroscopies, which span from investigations of magnetic and electronic properties, static and dynamic, and structural dynamics on various energy and time scales, to γ-optics and other fundamental research. Eventually, selected examples of applications will not only showcase the unique fields of research accessible with nuclear resonance techniques but also look in the bright future with the new light sources at the horizon.

1.1.1 Nuclear Resonance

Nuclear Resonance Scattering (NRS) with synchrotron radiation (SR) combines the outstanding properties of the Mössbauer effect with those of synchrotron radiation. Since its first convincing observation in 1984 [8] a rapid development of the technique with many facets followed. Thanks to the outstanding properties of 3rd generation synchrotron radiation sources nuclear resonance techniques are nowadays known for their extreme energy resolution and timing properties offering a wide range of applications.

Nuclear resonance techniques including Mössbauer spectroscopy are related to the recoiless resonant scattering, absorption, and emission of x-rays and γ-rays[1] by atomic nuclei. This effect is the same as in the atomic shell and well known e.g. from the yellow emission lines of sodium where light is absorbed and re-emitted by a transition of an electron between the 3p and the 3s atomic levels. Though the basics

[1] we use the term γ-ray for x-rays coming from a nucleus.

are the same nuclear resonance scattering was only discovered by Mößbauer in 1958 [1]. What are the reasons for this late discovery?

There are some important differences in the scattering of "optical" x-rays and γ-rays. First of all the transition energies E_0 are in the range of 1–10 eV and 10–100 keV, respectively. Further, the relative energy width $\Delta E/E_0$ of the involved atomic and nuclear levels are quite different partly due to the different excitation energies. As a consequence the recoil connected with the absorption and emission of a photon is a special problem for γ-rays because their recoil energy is so large that there is virtually no overlap of the absorption and emission lines in single atoms.

The recoil energy E_R is given as

$$E_R = \frac{E_\gamma^2}{2Mc^2} \,, \tag{1.1}$$

with $E_\gamma \cong E_0$ the photon energy, M the atomic mass, and c the velocity of light. For a typical Mössbauer isotope, e.g. ^{57}Fe with $E_0 = 14.4\,\mathrm{keV}$ and $M \approx 57\,\mathrm{u}$,[2] the resulting recoil energy is 1.956 meV, which is about six orders of magnitude bigger than the natural line width Γ_0 of its nuclear level ($\Gamma_0 = 4.66 \cdot 10^{-9}\,\mathrm{eV}$). On the other hand for the abovementiond sodium case ($E_0 \approx 2\,\mathrm{eV}$ and $M \approx 22\,\mathrm{u}$) the loss in energy due to recoil is virtually zero ($E_R \approx 10^{-11}\,\mathrm{eV}$). Finally, the thermal motion and the resulting Doppler broadening of the absorption and emission lines is another important aspect. Consequently, there exists full overlap in case of optical x-rays and no overlap for γ-rays. The achievement of R. L. Mößbauer was the understanding that, when an atom is bound in a solid, the entire solid ($M \to \infty$) will take the recoil and then the energy loss for the γ-ray is negligible. However, also in a solid vibrations of the atoms exist around their equilibrium position. R. L. Mößbauer showed that with a certain probability, expressed by the Lamb-Mössbauer factor (f_{LM}), no vibrations will be involved in the scattering, absorption, and emission process, respectively.

In order to shed some more light on this discovery and the f-factor we have to discuss some basic features of scattering. Generally for resonant scattering, the coherent elastic scattering amplitude f_{res} is given by [9]

$$f_{res} = \left(\frac{\Gamma_\gamma}{2ik}\right) \int_0^\infty \mathrm{d}t\, \mathrm{e}^{\mathrm{i}(\omega-\omega_0)t}\, \mathrm{e}^{-(\Gamma/2\hbar)t} \langle \mathrm{e}^{-\mathrm{i}\mathbf{k}_f\,\mathbf{r}(t)}\, \mathrm{e}^{\mathrm{i}\mathbf{k}_0\,\mathbf{r}(0)} \rangle, \tag{1.2}$$

where Γ_γ and Γ is the radiative and total resonance linewidth, respectively, $\hbar\omega_0 = E_0$ the resonance energy, $\mathbf{k}_0$ and $\mathbf{k}_f$ the wave vectors of the incident and reflected wave, respectively, and $\mathbf{r}(0)$ and $\mathbf{r}(t)$ are the displacement from the equilibrium position of the interacting particle at times zero and t, respectively. The $\langle\rangle$ represents the time average over the characteristic interaction times.

[2] Unified atomic mass unit $\mathrm{u} \mathrel{\hat{=}} 931.494\,\mathrm{MeV}/c^2$.

Zero point and temperature motion of a scatterer (e.g. atom or nucleus) are characterized by vibration times $\omega_m^{-1} \approx 10^{-14}$–$10^{-13}$ s. They have to be compared with the characteristic scattering times.

For resonant x-ray scattering, the characteristic scattering times are about 10^{-16}–10^{-15} s and hence fast compared to ω_m^{-1}, i.e., $t \to 0$ and the displacements from the equilibrium position can effectively be taken at $t \approx 0$, hence

$$\langle \mathrm{e}^{-\mathrm{i}\mathbf{k}_f\,\mathbf{r}(t\approx 0)}\,\mathrm{e}^{\mathrm{i}\mathbf{k}_0\,\mathbf{r}(0)}\rangle \approx \langle \mathrm{e}^{-\mathrm{i}[(\mathbf{k}_f-\mathbf{k}_0)\,\mathbf{r}]}\rangle = \mathrm{e}^{-\frac{1}{2}\langle[(\mathbf{k}_f-\mathbf{k}_0)\,\mathbf{r}]^2\rangle}. \tag{1.3}$$

This is the well known expression for the Debye-Waller factor f_D.

On the contrary, for Mössbauer resonances the scattering is slow, about 10^{-9}–10^{-6} s, compared to ω_m^{-1}, i.e., $t \to \infty$ and the displacements from the equilibrium position can effectively be considered as uncorrelated, hence

$$\langle \mathrm{e}^{-\mathrm{i}\mathbf{k}_f\,\mathbf{r}(t\approx\infty)}\mathrm{e}^{\mathrm{i}\mathbf{k}_0\,\mathbf{r}(0)}\rangle \approx \langle \mathrm{e}^{-\mathrm{i}\mathbf{k}_f\,\mathbf{r}}\rangle\langle \mathrm{e}^{\mathrm{i}\mathbf{k}_0\,\mathbf{r}}\rangle = \mathrm{e}^{-\langle x^2\rangle\,E_\gamma^2/(\hbar c)^2}\,, \tag{1.4}$$

with $\langle x^2\rangle$ the expectation value of the squared vibrational amplitude in the direction of the γ-ray propagation, the so-called mean-square displacement [10]. This expression is called the Lamb-Mössbauer factor f_LM. Equation 1.4 immediately shows that f_LM gets very small at higher energies, i.e., for practical reasons only nuclei with low lying nuclear levels ($\lesssim 100$ keV) are considered as Mössbauer nuclei.

In order to describe the f_LM one would need a detailed and comprehensive description of the phonon spectrum of the solid lattice. In general that is not available and for most cases the simpler Einstein or Debye model is sufficient to describe for example the temperature dependence of the Lamb-Mössbauer factor [10].

$$f_\mathrm{LM}(T) = \exp\left[\frac{-3E_\lambda^2}{k_B\Theta_D Mc^2}\left\{\frac{1}{4}+\left(\frac{T}{\Theta_D}\right)^2\int_0^{\Theta_D/T}\frac{x}{\mathrm{e}^x-1}\mathrm{d}x\right\}\right], \tag{1.5}$$

with Θ_D the Debye temperature and k_B the Boltzmann constant. Inspection of Eq. 1.5 reveals that a large f_LM is expected for low transition energies, low temperatures, and high Debye temperatures.

Due to the sharp width of the nuclear levels and their large separation, compared to atomic levels, the linewidth of the radiation for nuclear resonant scattering, absorption, and emission is a Lorentzian curve as given by the so-called Breit-Wigner equation:

$$I(E) = \frac{\Gamma_0/(2\pi)}{(E-E_0)^2+(\Gamma_0/2)^2}\,, \tag{1.6}$$

with the natural linewidth $\Gamma_0 = \hbar/\tau_0$ (τ_0 the natural lifetime) of the nuclear level. At resonance the scattering amplitude may peak much higher than for atomic scattering, e.g. for ^{57}Fe as $440\,r_0$ with $r_0 = 2.810^{-15}$ m the classical electron radius [9].

The discovery by R. L. Mößbauer made available a hard γ-ray source with unprecedented energy resolution $\Delta E/E_0 \approx 10^{-13}$ and longitudinal coherence length $l = c\,\tau_0 \approx 40\,\mathrm{m}$ in case of ^{57}Fe even nowadays only comparable with highest precision laser systems. Those properties made applications such as wavelength standard [11], Hanbury Brown-Twiss [12], interferometry [13, 14], and Lamb shift [15] feasible. Furthermore, they established spectroscopies on an atomistic scale, which are element and even isotope sensitive and non-destructive. Applications comprise two main fields, *hyperfine spectroscopy* and *structural dynamics*. In hyperfine spectroscopy NRS is complementary to other nuclear techniques and yields useful information on atomic, magnetic, and electric properties. Those fields of applications benefit most, which exploit the specific properties of synchrotron radiation and therefore allow for applications to high pressure, to grazing incidence geometry (surfaces and multilayers), to single crystals, and to very small samples. Structural dynamics on a ps to μs time scale as free or jump diffusion as well as rotational motions can directly be measured in the time domain by nuclear quasi-elastic scattering techniques. On the fast time scale the (partial) phonon density of states is directly accessible by (nuclear) inelastic scattering techniques.

For the application two cases may be distinguished, (i) excitation of the nuclear levels by 'white' SR with sharp pulses in time (ps) and the successive spectroscopy in the time domain and (ii) excitation of the nuclear levels by highly monochromatized radiation (energy width neV to peV defined by the nuclear level width Γ_0) with 'long' pulses in time (ns to μs) and the successive spectroscopy in the energy domain. Both are, generally speaking, connected by the Heisenberg uncertainty principle.

A comprehensive overview on the technique, experimental and theoretical, as well as on applications is given in the review book by Gerdau and de Ward [16]. The theoretical background was laid by Hannon and Trammell [17, 18] and Afanas'ev and Kagan [19, 20]. A detailed overview on optics may be found by Shvyd'ko [21] and on Nuclear Condensed Matter Physics by Röhlsberger [22]. An introduction to Mössbauer spectroscopy with applications is given by Gütlich, Bill, and Trautwein [10].

1.1.2 Synchrotron Radiation

Synchrotron radiation became a synonym for all electromagnetic radiation generated by transverse acceleration of relativistic charged particles. The name dates back to its first observation in the General Electric 70 MeV synchrotron. In contemporary synchrotron radiation facilities the particles are accelerated to their nominal energy by linear accelerators (linacs) and circular accelerators (synchrotrons). Eventually, the particles are fed into the storage ring where they travel on a stable, closed orbit and with fixed energy. This procedure allows for defined and optimum properties of the generated SR for the various applications.

The transverse acceleration in the storage ring is achieved by static transverse magnetic fields acting on charged particles such as electrons and positrons (see Fig. 1.1). For an electron, i.e., a particle of charge $-$e and of momentum $\mathbf{p} = m \cdot \mathbf{v}$,

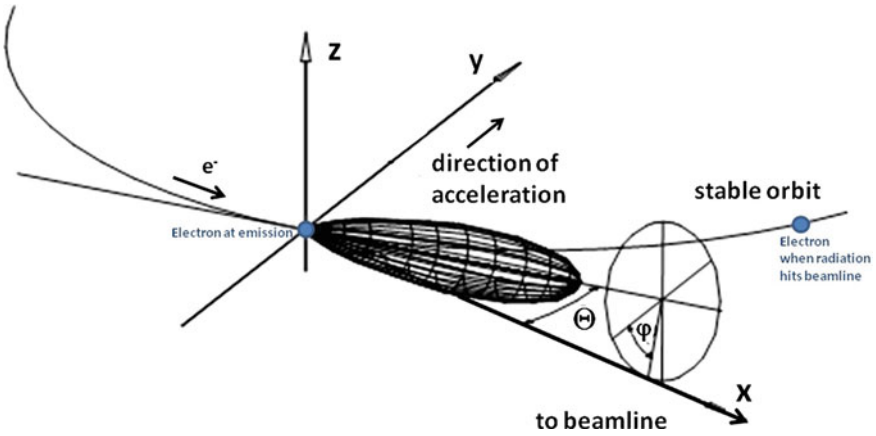

Fig. 1.1 Geometry of the synchrotron radiation. The acceleration points to the center of the storage ring. The radiation peaks in direction of the beamline in the $d\Omega = d\Theta\, d\phi$ cone. Note: The electron emits SR at the origin position and will be at the indicated position when that SR arrives at the beamline

with **v** its velocity and m its mass, the acceleration $\dot{\boldsymbol{v}}$ by a transverse magnetic field **B** is given by the Lorentz force $\mathbf{F}_L$:

$$\mathbf{F}_L = \frac{\mathrm{d}\mathbf{p}}{\mathrm{d}t} = -e \cdot [\mathbf{v} \times \mathbf{B}]\,. \tag{1.7}$$

Because the acceleration $\dot{\boldsymbol{v}}$ fully determines all characteristics of the emitted radiation, the synchrotron radiation can be purpose-engineered by selecting the type of particle, the particle current, the particle energy, and the spatial configuration of the magnetic fields. With that the resulting synchrotron radiation can be tailored in frequency, polarization, time structure, source sizes, and emission angles.

In case that the accelerating particles are at rest in the frame of the observer, like the electrons in an antenna, the radiated power P in the solid angle $d\Omega = d\Theta d\phi$ is given by classical non-relativistic electrodynamics:

$$\frac{\mathrm{d}P}{\mathrm{d}\Omega} = \frac{e^2}{4\pi c^3} \cdot \dot{v}^2 \cdot \sin^2\Theta, \tag{1.8}$$

and the total radiated power is given by

$$P = \frac{2}{3}\frac{e^2\dot{v}^2}{c^3} \qquad (Larmor formula). \tag{1.9}$$

The emission is characterized by:

(i) maximum power is radiated perpendicular to the direction of the acceleration,
(ii) there is zero radiation in the direction of acceleration, and

(iii) the polarization is along the direction of acceleration.

The for us interesting situation is the case where the velocity **v**, close to the velocity of light, is perpendicular to the acceleration $\dot{\boldsymbol{v}}$ of the emitting charge, i.e., relativistic charged particles in a transverse magnetic field in a circular particle accelerator: here the relativistic contraction of the emitted radiation is around the direction of maximum emission of the "antenna", while in the case where velocity **v** and acceleration $\dot{\boldsymbol{v}}$ are parallel (e.g. in a linear accelerator) the emitted radiation in forward direction would be zero.

The Lorentz transformation of the non-relativistic emission [23] leads to a contraction of the emission parallel to the velocity of the charge, which can be approximated for highly relativistic particles of total energy E by

$$\frac{\mathrm{d}P}{\mathrm{d}\Omega} \simeq \frac{2e^2\dot{v}^2}{\pi c^3}\,\gamma^6 \cdot \frac{1}{(1+\gamma^2\Theta^2)^3}\left[1 - \frac{4\gamma^2\Theta^2\cos^2\phi}{(1+\gamma^2\Theta^2)^2}\right] \tag{1.10}$$

and to an enhancement by a factor γ^4 ($\gamma = E/mc^2$ with m the rest-mass of the charged particle) of the emitted power P compared to the non-relativistic case as in Eq. 1.9:

$$P = \frac{2}{3}\frac{e^2\dot{v}^2}{c^3} \cdot \gamma^4. \tag{1.11}$$

Furthermore, the radiation appears in the laboratory frame highly collimated in a forward cone with an angle

$$\Delta\Theta = \pm\frac{1}{\gamma}. \tag{1.12}$$

This opening angle $\Delta\Theta$ defines for an observer the length L and duration Δt of the synchrotron light pulse, respectively:

$$L = \frac{4}{3}\frac{\rho}{\gamma^3} \quad \text{and} \quad \Delta\mathrm{t} = \mathrm{L/c}, \tag{1.13}$$

with ρ the radius of the curved path of electrons.

1.1.2.1 Emittance and Brilliance

The emittance and the brilliance are the two key parameters, which are nowadays used, to compare synchrotron radiation sources.

The emittance of a beam is defined as the area, enclosed by the one σ line,[3] of the particle density distribution. In case of zero emittance, i.e., an ideal beam, all particles travel on the closed orbit, which is given by the magnetic lattice and the nominal energy of the particles. The cross-section of this beam is pointlike and its divergence is zero. In this ideal case the synchrotron radiation from a given point shows the characteristics of single particle synchrotron light emission. This situation is called diffraction limited (dl).

Point size σ_{dl} and minimum divergence σ'_{dl} for light of wavelength λ are given under Gaussian approximation by

$$\sigma_{\mathrm{dl}} = \frac{\sqrt{L\lambda}}{2\pi} \quad \text{and} \quad \sigma'_{\mathrm{dl}} = \sqrt{\frac{\lambda}{L}}, \tag{1.14}$$

with L the apparent axial extension of the source [24]. This apparent axial extension could be either the undulator length in the case of an undulator source (see Sect. 1.1.2.3) or the particle's path length needed for a deflection of $\Delta\Theta = 2/\gamma$ in a bending magnet source (Eq. 1.13). In such a case of a "diffraction limited synchrotron light source" each phase space occupied by the synchrotron light beam (photon emittance) would be with $i = x, y$

$$\varepsilon_{\mathrm{dl,i}} = \sigma_{\mathrm{dl,i}} \cdot \sigma'_{\mathrm{dl,i}} = \frac{\lambda}{4\pi}. \tag{1.15}$$

For undulator radiation these values are first approximations and may need modifications accounting e.g. for non-Gaussian profiles (see e.g. [25]).

The dimensions for the electron beam may be calculated in first approximation—without considering dispersion and energy spread—by the following expressions, with ε_i the emittance and β_i the β-function of the lattice ($i = x, y$):

$$\sigma_i = \sqrt{\varepsilon_i \cdot \beta_i} \quad \text{and} \quad \sigma'_i = \sqrt{\frac{\varepsilon_i}{\beta_i}}. \tag{1.16}$$

Eventually, the effective x-ray beam dimensions are then given by the convolution of these quantities with the diffraction limited values $\sigma_{\mathrm{dl,i}}$, $\sigma'_{\mathrm{dl,i}}$ of the X-ray beam:

$$\sigma_{\mathrm{T_i}} = \sqrt{\sigma_i^2 + \sigma_{\mathrm{dl,i}}^2} \quad \text{and} \quad \sigma'_{\mathrm{T_i}} = \sqrt{\sigma_i'^2 + \sigma'_{\mathrm{dl,i}}{}^2}. \tag{1.17}$$

The brilliance B is the peak flux density in phase space

$$B = \frac{\text{photons/s}}{\sigma_x \sigma_y \cdot \sigma'_x \sigma'_y \cdot d\varepsilon/\varepsilon}, \tag{1.18}$$

[3] All 'σ' values in this paragraph are 'root mean square' (rms) values assuming Gaussian distributions. They have to be multiplied by $2\sqrt{2\ln 2} \approx 2.355$ in order to get the corresponding 'full width at half maximum' values.

with σ_i in mm, σ_i' in mrad, and $d\varepsilon/\varepsilon$ in 0.1% energy bandwidth. In Anglo-American publications very often the brilliance is named "(spectral) brightness".

1.1.2.2 Time Properties

The energy loss of the particles due to the radiated power (synchrotron radiation) (see Eq. 1.11) has to be supplied back to keep the particles on their stable orbit. That is done by rf-transmitters and so-called cavities in the storage ring. The involved frequencies are in the UHF regime (352 MHz for the ESRF) and define together with the circumference of the ring the stable positions, called buckets, for the particles. In case of the ESRF with a circumference of 844 m 992 buckets are available to be filled with electrons separated by 2.8 ns. In principle any pattern of buckets, out of the 992, may be filled to allow for the necessary flexibility to the demand at the experimental stations. Those filled buckets are called bunches and are about 100 ps in length. Typical filling pattern at the ESRF are currently the multi-bunch mode (7/8 + 1: meaning that 7/8th of the ring is closely filled with 868 bunches plus a single bunch just in the center of the remaining gap leaving 176 ns empty space for timing experiments), 16 bunch mode (16 buckets are filled with a separation of 176 ns each), and 4 bunch mode (4 buckets are filled with a separation of 704 ns each).

Most of the NRS experiments rely on those two timing modes, 4- and 16-bunch mode. A special signal (bunch clock) is available for synchronizing this timing with the experimental needs. An important parameter is the "purity" of the filling. It is defined as the ratio between the number of photons emitted by electrons in accidentally filled buckets and the number of photons emitted by the electrons of the nominal bunches. Routinely a purity better than 10^{-9} up to 10^{-11} is reached by special cleaning procedures at the ESRF.

1.1.2.3 Insertion Devices

So far we have only considered the bending magnets, responsible for the transverse acceleration and for keeping the particles on a closed orbit, as a source for synchrotron radiation.

Third generation SR sources are however characterized by their additional synchrotron radiation sources, so called "insertion devices", special magnet structures inserted in dedicated "straight sections" of the storage ring. Their properties may be tailored to the needs of the experimental stations. The most simple case is a planar magnet structure of alternating short dipole magnets, see Fig. 1.2. They are arranged such that the field varies sinusoidally along the particle trajectory

$$B(x, y = 0, z = 0) = B_0 \cdot \cos\left(\frac{2\pi}{\lambda_u} \cdot x\right), \tag{1.19}$$

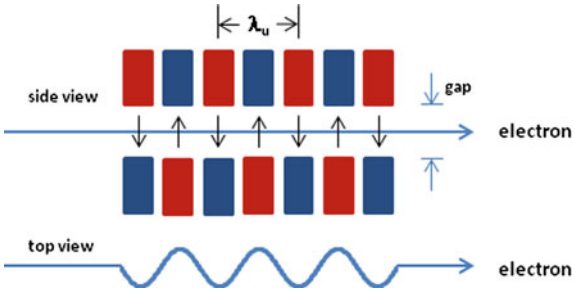

Fig. 1.2 Schematics of an insertion device. Top panel: side view of the alternating dipole magnets (red: north pole, blue: south pole) with the electron beam traveling in the center with λ_u the magnetic period and gap the magnetic gap of the undulator. Bottom panel: top view of the sinusoidal electron movement due to the alternating magnetic field. The amplitude is not to scale and is in the order of microns

with B_0 the peak magnetic field and λ_u the magnetic period. The particle will then oscillate with the amplitude

$$y(x) = \frac{K}{\gamma\, 2\pi/\lambda_u} \cos\left(\frac{2\pi}{\lambda_u} \cdot x\right), \tag{1.20}$$

with $K = \frac{ecB_0\lambda_u}{2\pi mc^2}$ the so called deflection or strength parameter. For $K \gg 1$ the insertion device is called a wiggler and for $K \ll 1$ an undulator. The (magnetic field) strength can be varied by changing the magnetic gap height, which in turn will change the K value and eventually the wavelengths (energies) of the SR spectrum.

Nowadays, mainly undulators will be used, which allows one to optimize the photon beam quality such as its brilliance, energy spectrum, signal-to-noise ratio or to provide special chracteristics such as dedicated (elliptical, circular) polarizations.

For the various harmonics k of an undulator the dependence on K and λ_u can be expressed in photon wavelengths λ as:

$$\lambda_k = \frac{\lambda_u}{2\gamma^2 k}\left(1 + \frac{1}{2}K^2 + \gamma^2\Theta^2\right), \tag{1.21}$$

and in photon energies ε as:

$$\varepsilon_k = \frac{4\pi\hbar c\gamma^2 k}{\lambda_u\left(1 + \frac{1}{2}K^2 + \gamma^2\Theta^2\right)}. \tag{1.22}$$

In this paragraph we could only mention those quantities, which are most important with respect to NRS experiments. There exist a waste amount of literature, which treats all aspects of SR, such as the review work by Wiedemann [24] with references therein.

1.2 Historical Development

In this chapter we want—on the example of NRS with SR—to point out how research may evolve from first ideas and discussions to the hopefully successful finish. What are the scientific dreams, at the beginning and at the end of such an endeavour? What are the technical challenges? Are there other aspects, which were crucial for the development and the science of such a project? Eventually, we can report on the successful achievement of this endeavour: Nuclear Resonance Scattering with Synchrotron Radiation.

Even when there were already some discussions going on, the "kick-off" moment for nuclear resonance with synchrotron radiation was certainly the Mössbauer conference 1974 in Bendor (France). In his contribution Stan Ruby discussed synchrotron radiation as a new source for Mössbauer spectroscopy instead of radioactive sources [26]. It was at a time when SR was mainly a nuisance for the researchers doing high-energy physics with the new colliders using highly energetic electrons and positrons. This unavoidable SR prevented them to increase the particle energy to higher and higher values. Anyway, first attempts had already started to use that radiation in a parasitic manner e.g. for atomic and solid state physics. Now, also the Mössbauer community started with several groups all over the world trying to excite Mössbauer isotopes with SR.

1.2.1 Scientific Dreams

Of course the idea itself—creating a resonant Mössbauer beam out of the SR—is highly appealing and warrants to be tackled. That was for sure one of the important reasons to start the endeavour. On the other hand the discussions at that time show that the combination of the outstanding features of both, the SR and the MB effect, would make new experiments feasible either out of reach or deemed extremely difficult.

Diffraction experiments were named very early with emphasis on the "phase problem" [27]. The temporal coherence of the new source and superradiance has been mentioned as well [28]. In the course of the preparation for a dedicated SR source in Europe, a first set of experiments has been proposed [29]:

- **Analysis of the magnetic structure of complicated compounds** which would benefit from the defined polarization of the SR.
- **Time experiments** such as the observation of relaxation processes between hyperfine levels, the time dependence of the Debye-Waller factor, and the interference between the Mössbauer effect and the conversion or other competing processes. Even laser activation of the environment of the MB nuclei synchronous to the SR flash, nowadays known as pump-and-probe, has been proposed.
- **Nuclear γ-optics** which includes dichroism, magnetooptic effects such as double refraction and Faraday rotation. Further, the interference of the nuclear and the

electronic scattering, the nuclear Borrmann effect, and the suppression of the inelastic channel has to be mentioned.
- **Phase sensitive optics** will allow interference experiments with a large coherence length.
- **Gravitation experiment** in tribute of the very difficult and famous red-shift experiment by Pound and Rebka [30].
- **Small angle scattering**, known as small angle x-ray scattering (SAXS), may be expanded to the Mössbauer radiation to become sensitive as well to magnetic and electric domains/distributions.

This is an impressive list of topics, which was updated for the final technical design report of the ESRF [31]. Remarkable from a present-day perspective is the focus on investigations of "basic science" effects, spectroscopy is nearly absent. Looking back, the explanation might be simply the background of the involved people. They were mainly grown up in nuclear physics.

As we will witness in the Sects. 1.7 and 1.8 the development over the years went after all mainly in a different direction.

1.2.2 Technical Challenges

The main challenge was the unfavorable signal-to-noise-ratio. SR is thought to be a "white" radiation source, i.e., the energy band width of the radiation coming from the bending magnets of the synchrotron spans from literally "zero" to several tens keV. The low energy part could easily be absorbed, however, still a band width of let's say 20 keV was left. On the other side, in case of the 14.4 keV nuclear level in ^{57}Fe, the nuclear level width is 4.66 neV. That means a signal-to-noise-ratio of about 10^{-13}. How to find those resonant quanta in this haystack?

In the following we will discuss various ideas and avenues.

1.2.2.1 Time and Polarization Properties

As discussed above, SR is a pulsed radiation with pulse widths Δt in the 100 ps regime and—in principle—selectable repetition rate. That means that one may accordingly adopt the time structure to the life time τ_0 of the excited nuclear levels. Then it is possible to excite the nuclear levels instantaneously ($\Delta t < \tau_0$) and to record their de-excitation products such as γ-rays and conversion electrons inbetween the synchrotron radiation pulses. Due to the fact that electronic scattering processes are very fast one should see after very intense "prompt" scattering processes only the "slow" scattered γ-radiation from the scattering via the nuclear resonances. That means one would be able to generate out of the SR a pure beam of γ-radiation through time discrimination. Unfortunately, even with todays fast detector systems, it is vrtually impossible for the detectors to sustain the extreme count rates beyond 10^9 photons/s.

However, the time discrimination technique has widely been used as an additional option in the quest of the resonant quanta.

Similary, one might use the different polarization behaviour of electronic and nuclear resonance scattering. As discussed above, SR is linearly polarized in the plane of the synchrotron, i.e., the electric wave vector is parallel to the acceleration and perpendicular to the velocity of the particles. For horizontal (in-plane) 90°-scattering the electronic scattering (electric dipole (E1)) would be "zero", whereas e.g. in case of ^{57}Fe with its 1/2–3/2 magnetic dipole transition (M1) the nuclear scattering could stay due to optical activity. In the early days this could not efficiently be accomplished due to technical challenges. However, meanwhile with state-of-the-art SR sources and crystal optics this endeavour was successful reaching polarization purities in the 10^{-9} to 10^{-10} regime, see e.g. [32].

1.2.2.2 Thin Films and Total Reflection

Another method to suppress the electronic towards the nuclear scattering lies in the different strength of their scattering amplitudes. In case of ^{57}Fe the intensity of nuclear scattering is about 400 times bigger than the electronic one.

Trammell et al. [33] have calculated that in case of a 10^3 layer thick iron crystal only about three successive (332)-reflections would be sufficient to filter a pure γ-ray beam out of the SR. They assumed 90°-scattering in order to benefit as well from the different scattering properties, E1 and M1. However, to our knowledge no such experiment has been successfully conducted.

Staying with thin films, however now in total reflection geometry, one may even omit the need for single crystals. Then the key parameter is the different index of refraction for electronic and nuclear scattering. Further, one may coat the surface with a $\lambda/4$ anti-reflection layer, such as in optical applications, for an additional suppression of the electronic scattering. These are the so-called "Grazing Incidence Anti-Reflection" (GIAR) films [34]. Theory predicts suppression factors of 10^3–10^4. Various solutions have been discussed and laid down in several publications [35–38].

In practice those suppression values could not be reached at that time due to the rather big divergence and beam size of the SR and the non perfect big mirrors needed for total reflection. Nowadays with the improved and dedicated SR sources those ideas flourish e.g. in γ-optical applications, see Röhlsberger and Evers [39].

1.2.2.3 Pure Nuclear Reflections

The most promising avenue seemed to be nuclear Bragg diffraction (NBD) and the use of so-called pure nuclear reflections.

In contrast to the well-known Bragg diffraction at the electrons, electric charge scattering, now the scattering proceeds resonantly via the interaction of the radiation with the excited nuclear levels (Mössbauer levels). In consequence nuclear Bragg

diffraction is only possible at distinct energies, the Mössbauer transition energies, and therefore shows a very pronounced and complex resonance character.

The theoretical treatment of nuclear diffraction has independently been developed by two groups well before any thoughts went to SR. Trammell [40] mentioned first the possibility; later Kagan et al. [41], Afanas'ev and Kagan [19, 20], and Hannon and Trammell [17, 18] laid down the theory in detail.

Pure nuclear reflections are named such reflections, which are forbidden due to crystal symmetry, i.e., the electronic scattering amplitude is zero, but allowed for nuclear resonance diffraction due to a different symmetry caused by the properties of the Mössbauer nuclei. Intuitively this might be understood for a hypothetical crystal, which has alternative layers of ^{56}Fe- and ^{57}Fe-atoms with lattice constant d. For electronic scattering the lattice constant is d, because for both isotopes the number of electrons is the same, whereas for nuclear resonance scattering via the ^{57}Fe nuclear exited level the "Mössbauer lattice" constant is 2d. Choosing an appropriate Bragg angle the electronic scattering interferes destructively whereas the nuclear resonance scattering constructively giving rise to the pure nuclear reflection.

Already shortly after the discovery of the Mössbauer effect first diffraction experiments have been conducted with radioactive sources and pure nuclear reflections reported. Those may be classified in reflections due to accidential extinction and magnetic, electric, and combined magnetic and electric superstructures, respectively. Early examples may be found e.g. for an accidental reflection in the [080]-reflection of $K_4Fe(CN)_6{\cdot}3H_2O$ [42], for "magnetic" reflections in α-Fe_2O_3 [43] and $FeBO_3$ [44], for "electric" reflections in the (003)-reflection of $Na_2Fe(CN)_5NO{\cdot}2H_2O$ [45] and for tellur [46], and finally for "combined" reflections in $KFeF_4$ [47], yttrium-iron-garnet (YIG) [48], and Fe_3BO_6 [49].

1.2.3 Political Facts

It might be surprising to find here as well a paragraph on this issue, politics. However, we are very sure, looking back with our todays knowledge and the current scientific situation, that already at that time "politics" played a major role, in one or another way.

It was at a time were "impact factors" and "high-impact" journals have not yet played that important role as today. However, the budgetary situation became more crucial and more and more big scientific facilities competed with each other and with other projects. In the beginning, the endeavour of NRS with SR was thought to be on a short timescale. However, when it took longer and longer the funding was no longer granted on that time scale and most of the "beginners" had to stop the endeavour. Eventually, it was only the Hamburg group, which could convince the funding agencies to invest in "no results" for a long period of nine years, and eventually, it paid off. Would that still be possbile nowadays?

Another long-term issue was the discussion on dedicated SR sources. It became very early clear that the common use of those accelerators for high-energy physics

and synchrotron radiation based science, respectively, will never result in optimum conditions for both communities. Therefore, already shortly after first SR experiments in the 70th, discussions started e.g. in Europe for a dedicated high-energy SR source. This was as well an endeavour, which should finally last for more than a decade. The Mössbauer project was one of the very well adapted cases for such a high-energy source especially due to the high transition energies of nuclear levels. It really neededd a vision and courage to make the case for those early proposals of an European SR facility [29] without having seen any "resonant quanta"! However, it was important and essential and was rewarded with a first dedicated high-energy SR facility in the world, the ESRF, and a Mössbauer beamline, called later Nuclear Resonance beamline.

During the discussion of that facility and also later during the start-up and continuous operation a strong community was mandatory for a successful and promising future. This is nowadays even more important with all the frequent evaluations, comparisions between projects, and short term goals. Without such a community, the proper networking, and the endless fights even the best ideas are damned to fail. So far the nuclear resonance community is small and has to make up in the synchrotron radiation scene.

1.2.4 First Results—The Needle in the Haystack

In the course to find the needle in the haystack nearly every avenue described above, and may be more, has been tried over nearly a decade of unsuccessful attempts. However, only very few of those attempts have been reported and may be traced back [50].

Eventually, the pure nuclear reflection strategy brought the break-through in a more than expected and convincing clearness [8].

The measurements were conducted at the Mössbauer test station at HASYLAB located at the storage ring DORIS (Desy, Hamburg). DORIS was running in 2- and 4-bunch mode with 480 ns and 240 ns spacing, respectively, and provided SR from a bending magnet. The original experimental set-up is shown in Fig. 1.3. 22 m downstream of the source point the high-heat-load monochromator, two Ge (111) single crystals, monochromatized the SR at 14.4 keV with $\Delta E = 13$ eV. After the monochromator a beam size of 2 mm × 20 mm (v × h) was defined by a slit system and an intensity of about 10^9 photons/(mA s) measured. Eventually, $(3–6) \times 10^{10}$ 14.4 keV photons/s were available for the experiment.

The nuclear monochromator consisted of two 15-μm thick single-crystalline films of YIG (88% enriched in ^{57}Fe) epitaxially grown on the [100] surface of a gadolinium gallium garnet (GGG) single crystal with 30 mm in diameter. An amount of about 10 g ^{57}Fe, purchased over several years, and several years of discussion were necessary for the conviction and production of those films by the Philips research laboratory in Hamburg. The two crystals were aligned in non-dispersive, and with respect to the high-heat-load monochromator, in dispersive geometry. Both YIG crystals were set

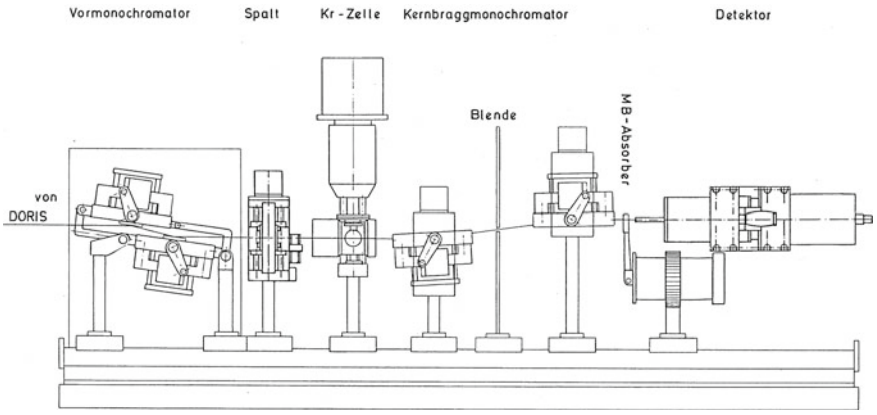

Fig. 1.3 Experimental set-up at the "Mössbauer Test station" F4 at DORIS, Desy (Hamburg) (from [51]). The entire set-up is about 2 m in length. Vormonochromator: high-heat-load monochromator, Spalt: slit system, Kr-Zelle: energy calibration with Kr K-edge, Blende: aperature, Kernbraggmonochromator: nuclear monochromator, MB-Absorber: MB-absorber on MB-driving system, Detektor: high-purity germanium solid state detector (cooled)

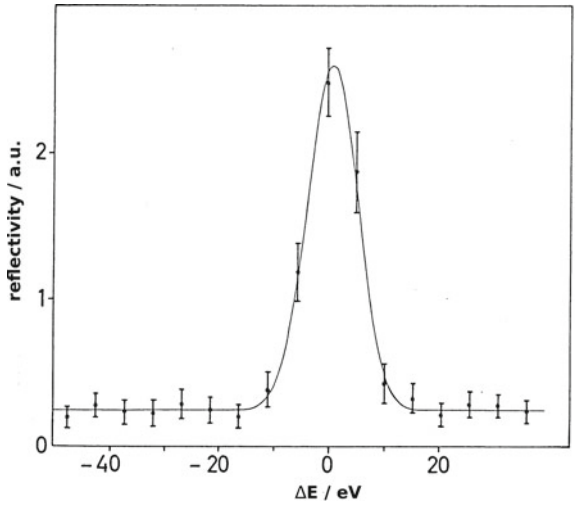

Fig. 1.4 Resonance curve of the diffracted γ-quanta after the nuclear monochromator as function of the energy of the high-heat-load monochromator. The solid line is a fit with a Gaussian distribution and the energy scale is centred to its maximum (from [51]). (Reprinted figure with permission from [8], Copyright (1985) by the American Physical Society)

to the [002] pure nuclear reflection. A small external magnetic field (30 mT) assured a defined and single domain magnetic state of the crystals.

As detector system a high-purity germanium solid state detector with about 1 keV energy resolution and a conventional fast-slow coincidence system (see Fig. 1.14) with an overall 18 ns time resolution has been used.

The performance of the system was verified by measuring the so-called resonance curve of the nuclear monochromator, i.e., the intensity of the resonant quanta, as integrated over a time window between 32 and 137 ns after the prompt pulse, versus the energy of the system. Figure 1.4 displays the reflectivity of the nuclear monochro-

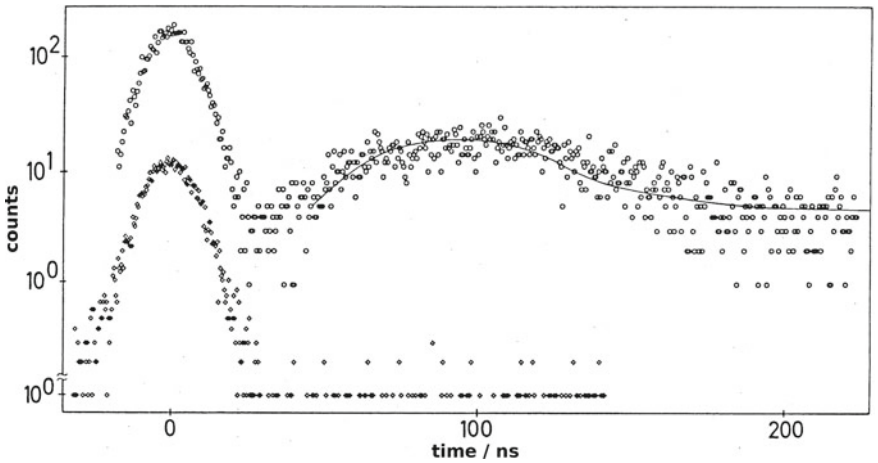

Fig. 1.5 Time spectra of the diffracted γ-rays after the nuclear monochromator on resonance (upper curve) and off resonance (lower curve). The solid line is a fit with the dynamical theory of NBD (from [51]). (Reprinted figure with permission from [8], Copyright (1985) by the American Physical Society)

mator versus the energy defined by the high-heat-load monochromator. The energy width of 10.13(5) eV is determined by the widths of the germanium and YIG crystal reflections and their dispersive geometry.

The time spectra after the nuclear monochromator consist of a "prompt" component, certainly due to residual background radiation and Umwegreflections, and, on resonance, of the delayed nuclear scattering response, see Fig. 1.5. The solid line through the delayed component has been calculated with CONUSS applying the dynamical theory of NBD [53] accounting for a two-crystal arrangement.

Finally, a Mössbauer spectrum proved in another way the existence of resonant quanta (Mössbauer quanta). A stainless steel single-line absorber (1 mg ^{57}Fe/cm^2) on a conventional MB-driving system was installed downstream of the nuclear monochromator, see Fig. 1.3. The resulting spectrum after about 30 h of effective measuring time is shown in Fig. 1.6. The remarkable high effect ($\sim$40%) allowed even with the low count rate of 0.5 Hz for a clear spectrum. The theory (solid line) resembles nicely the measured spectrum.

With these three proofs, undoubtedly, a 1-Hz beam of nearly pure resonant γ-quanta was now available for further experiments. And indeed, these results again triggered a new rush not only to use but also to improve and develop this technique as it is shown in the following sections.

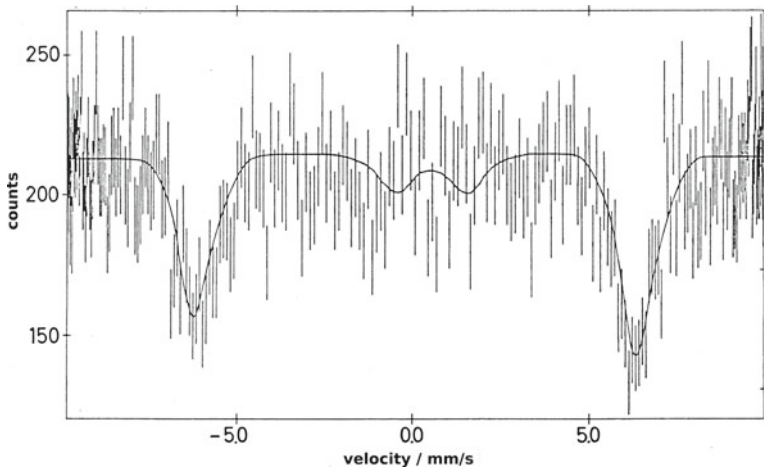

Fig. 1.6 Mössbauer absorption spectrum after the nuclear monochromator with a thick stainless steel absorber. The solid line is a fit with the dynamical theory (from [51]). (Reprinted figure with permission from [8], Copyright (1985) by the American Physical Society)

1.3 Techniques in NRS

After these first experiments several groups with different expertise in more technical fields such as high resolution crystal optics, fast detector systems, synchrotron radiation, nuclear resonance scattering as well as in various fields of applications newly started with nuclear resonance scattering with synchrotron radiation. A very fruitful and successful synergy emerged from this combined expertise and effort, which are summarized, not in historical order, in this chapter.

1.3.1 Synchrotron Mössbauer Source

The Synchrotron Mössbauer Source (SMS), see Fig. 1.7 SMS, provides a 100% resonant, polarized, and collimated γ-ray beam for high energy-resolution applications and energy domain Mössbauer spectroscopy, furtheron called SMS spectroscopy. The high energy resolution ($\Delta E \sim$ neV) is achieved by nuclear monochromators based on nuclear Bragg diffraction from pure nuclear reflections rather than by radioactive sources. In both cases the resolution is governed by the natural line width Γ_0 of the concerned nuclear level. First attempts towards a SMS were already published [8, 54, 55] in the early days of NRS. The breakthrough came with dedicated SMSs for the Mössbauer isotope of ^{57}Fe, utilizing $^{57}FeBO_3$ single crystals as nuclear monochromator, at various beamlines [56, 57]. Since that time SMS spectroscopy flourish with numerous applications.

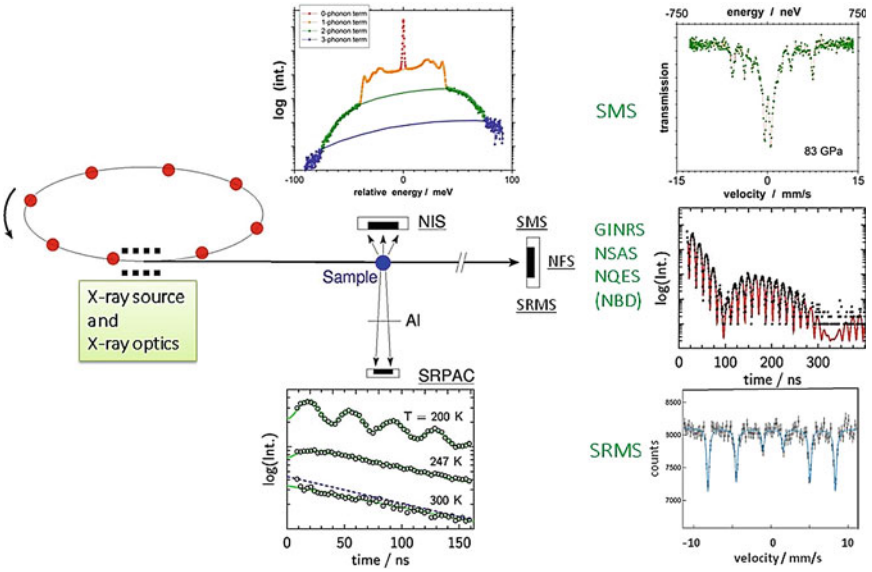

Fig. 1.7 Scheme of the set-up for some techniques in NRS: SMS, SRMS, NFS, NIS, and SRPAC. Furthermore, the corresponding time and energy spectra are schematically shown measured by the detectors for SMS-NFS-SRMS, SRPAC and NIS. For time resolved measurements and SRMS the storage ring is operated in *few bunch* mode with e.g. 176 ns spacing between adjacent buckets at the ESRF (red bullets). For measurements with the SMS timing mode is not an issue and any filling mode may be used. The x-ray source, nowadays an undulator, produces the well collimated synchrotron radiation, which is monochromatized at the nuclear resonances by dedicated x-ray and γ-ray optics with bandwidths ranging from eV to neV. Finally the radiation impinges on to the sample. Depending on the scattering process and the scattering geometry different techniques are exploited. Variable sample environments allow for the combination of high/low temperature, high pressure, and external magnetic field

In contrast to traditional Mössbauer spectroscopy, the energy spectrum of the radiation emitted by the $^{57}FeBO_3$ single crystal of the SMS is the result of the interference of two spectral lines (each with a Lorentzian distribution, Eq. 1.6) with almost equal resonance energies. Therefore, the energy spectrum of the radiation emitted by the SMS is a squared Lorentzian distribution rather than a single Lorentzian [58]:

$$I(E) = \left[\frac{\Gamma_0/(2\pi)}{(E - E_0)^2 + (\Gamma/2)^2} \right]^2 , \tag{1.23}$$

where Γ is the width of each of the interfering lines, E is the energy of radiation, and E_0 is the resonance energy. The knowledge of the exact shape of the energy distribution, i.e., the instrumental function, is mandatory for proper data evaluation. Furthermore, the radiation is fully polarized with the electric wave field in the vertical plane.

Normally, spectroscopy is carried out in transmission geometry as in conventional Mössbauer spectroscopy with radioactive sources. In both cases the energy of the γ-quanta is varied via Doppler shift in the neV to μeV regime by moving the source and after the sample the energy spectrum is recorded. The excellent collimation of the γ-ray beam from the SMS allows as well for scattering experiments, which were very challenging with radioactive sources due to their isotropic emission spectrum and only exceptionally done.

Sofar the SMS has been developed for the case of ^{57}Fe, which was favoured due to the availability of highly perfect single crystals enriched in the Mössbauer isotope. However, generally speaking, this may be achieved for any Mössbauer isotope provided one is able to grow perfect single crystals or structures, which show pure nuclear reflections and preferably a single line.

1.3.2 Synchrotron Radiation Based Mössbauer Spectroscopy

Another technique in the energy domain was recently presented by Seto et al. [59]: Synchrotron radiation based Mössbauer spectroscopy (SRMS), see Fig. 1.7. The idea is as follows: The sample under investigation (in the beam) "modulates" the synchrotron radiation, which is then analyzed (demodulated)—by time integration and an efficient resonance detector—in the energy domain utilizing a conventional Mössbauer driving system. In order to improve the signal-to-noise-ratio timing mode is still required for the suppression of the prompt radiation by time-gating. That implies that the time integration can only be carried out over a finite time window, which in turn influences the energy spectrum. A detailed description will be given elsewhere in this book by Seto et al. [60].

1.3.3 Nuclear Forward Scattering

Nuclear forward scattering [61, 62] may be considered as the time analog to Mössbauer spectroscopy; in fact it is its scattering variant. The 'white' synchrotron radiation excites all Mössbauer levels in the sample and creates a *coherent collective nuclear state*. In the static case this nuclear state will decay in the forward direction giving rise to an excess of intensity at delayed times (see Fig. 1.7 NFS). The time scale is determined by the lifetime τ_0 of the involved nuclear level. Multiple scattering may influence the measured time response giving rise to *dynamical beats*. Furthermore, in case of split nuclear levels due to hyperfine interaction (electric, magnetic) an additional interference pattern from all involved nuclear levels, the so-called *quantum beat* structure is superimposed.

An important variant of NFS is reflectometry or grazing incidence nuclear resonance scattering (GINRS) for the investigation of thin films, surfaces etc. Even when the scattering angle in GINRS is very small (mrad) one has to account for it in

the evaluation of the spectra due to an enhancement of the effective thickness (see Sect. 1.4.2) by interference effects and the grazing incidence geometry.

Small structures such as magnetic and electric domains may give rise to nuclear small-angle scattering (NSAS) [63, 64]. Recording both, the prompt (charge) scattered signal and the delayed (nuclear) one, one easily distinguishes between structural and magnetic/electric structures.

1.3.4 Synchrotron Radiation Based Perturbed Angular Correlation

For the techniques described above, SMS spectroscopy, SRMS, and NFS, the Lamb-Mössbauer factor has to be greater than zero in order to apply those spectroscopies. As discussed in Sect. 1.1 that might not be the case for samples at high temperature, for liquids and gases, or for nuclei with high energetic transitions.

Then the spatially incoherent channel of nuclear resonant scattering, which is independent of the Lamb-Mössbauer factor, offers a way out of these difficulties via Synchrotron Radiation based Perturbed Angular Correlation (SRPAC) [65, 66] (see Fig. 1.7 SRPAC). It can be considered as a scattering variant of time differential perturbed angular correlation (TDPAC) [67]. In SRPAC, on the contrary to NFS, the nuclear levels are excited from the ground state during incoherent, single-nucleus resonant scattering of SR. The interference of indistinguishable paths via these intermediate nuclear levels, split by magnetic dipole and/or electric quadrupole interaction, allows one to investigate hyperfine interactions $\hbar\Omega$ and spin dynamics.

The scattering intensity can be written as

$$I_{\mathrm{SRPAC}}(t) = I_0\, \mathrm{e}^{-t/\tau_0}\{1 - A_{22}G_{22}(t)\} \tag{1.24}$$

with A_{22} the anisotropy and angular term and G_{22} the perturbation factor.

SRPAC can be applied to all nuclei with an isomeric state with energies attainable by synchrotron radiation, so far, for practical reasons, with energies up to 150 keV. In addition, also the contrast of the SRPAC signals might be much larger than for TDPAC since unfavourable transitions to the excited states from above can be avoided. Furthermore, the SRPAC technique can be used in a site-selective option [68].

1.3.5 Time Interferometry and Rayleigh Scattering

For samples without Mössbauer isotopes, in addition to fast (phonon) dynamics accessible with IXSNRA (Sects. 1.3.6.2 and 1.5.2) one may also retrieve slow relaxation (ps to ms time scale) dynamics. This is done in the time domain with time

domain interferometry (TDI) [69] and in the energy domain with Rayleigh scattering with Mössbauer radiation (RSMR) [70, 71].

The TDI setup includes the sample under investigation and two resonance absorbers. The first one is placed in the path of the incident radiation upstream of the sample and the second one downstream of the sample in the path of the scattered radiation at the defined momentum transfer under investigation.

In the default scheme [69], these are single-line absorbers. One of those is at rest, the other one is driven by a MB transducer with constant velocity, defining the difference in the energies of the two nuclear resonance transitions. A partial probability of nuclear forward scattering of each photon by the upstream and downstream absorbers gives the probe and the reference wave, respectively.

In absence of slow dynamics, nuclear forward scattering from both samples proceeds elastically, and an interference of the probe and reference waves displays quantum beats, defined by the difference in the resonance energies of the two absorbers.

Under relaxation conditions, nuclear forward scattering of the probe wave acquires with time a phase shift, which damps the beats. The envelope of the fading contrast of the quantum beats provides the momentum-transfer dependent auto-correlation function of the density fluctuations (intermediate scattering function) [69].

For the RSMR set-up a radioactive source or a nuclear monochromator, the SMS, prepares a high-resolution γ-ray beam and after the sample a resonance detector analyzes the scattered radiaton at the defined momentum transfer under investigation. In absence of dynamics the MB spectrum resembles the source characteristics whereas in case of dynamics the line width will broaden according to the dynamics.

A detailed description of RSMR with SR will be given elsewhere in this book by Seto et al. [60].

1.3.6 Inelastic Scattering

1.3.6.1 Nuclear Inelastic Scattering

Nuclear inelastic scattering [72] measures the *(partial) phonon density of states* (DOS) of the Mössbauer element in the sample [72–74]. The principle set-up is shown in Fig. 1.7 NIS.

The synchrotron radiation is monochromatized by a high resolution monochromator (HRM) with (sub-) meV energy resolution. At resonance the x-ray pulse creates a coherent collective nuclear state as in NFS, which decays either in forward direction or incoherently, due to internal conversion, spin flop etc., in the entire solid angle of 4π. This feature gives a simple and effective method at hand to measure the instrumental function (detector NFS) in parallel with the inelastic spectrum (detector NIS). While scanning the HRM the nuclear resonance can be excited when at the same time a phonon is created or annihilated. In NIS this is a purely incoherent process with a perfect averaging over the momentum $\mathbf{q}$. The successive nuclear decay proceeds as

a single exponential in the entire solid angle covered by the '4π'-detector (detector NIS). In practice only a solid angle of about π can be achieved.

1.3.6.2 Inelastic X-Ray Scattering with Nuclear Resonance Analysis

NIS needs the Mössbauer isotope in the sample. Phonons in samples not containing Mössbauer isotopes may be studied with "Nuclear Resonance Energy Analysis of Inelastic X-Ray Scattering" (IXSNRA) [75]. In this case the set-up resembles the classical three-axes-spectrometer for inelastic scattering experiments consisting of the monochromator, sample, and analyzer. Nevertheless, the set-up looks like that for NIS (see Fig. 1.7 NIS). However, the (energy) analysis is now carried out with a "resonance detector" containing the Mössbauer isotope as a high-resolution analyzer.

1.3.7 Other Techniques

There exist some other techniques and extensions related to NRS. They can not be discussed here in detail, however, for further reading they are cited (the first publication) in the following.

Everything started with Nuclear Bragg Diffraction [8], however, little has been done during the past decades [76–78].

Several techniques have been developed in order to overcome the need for high-resolution x-ray optics and for dedicated timing modes such as the lighthouse effect [79, 80], stroboscopic detection of nuclear resonance [81], polarimetry [82–84], μeV-resolved spectroscopy [85].

1.4 Hyperfine Spectroscopy

Hyperfine spectroscopy, i.e., the investigation of electric and magnetic properties, can be carried out with the SMS, SRMS, NFS, and SRPAC. The SMS and (partly) SRMS, like the conventional Mössbauer source, probes with its narrow energy bandwidth the nuclear hyperfine splitting of the levels one by one in the energy domain whereas NFS and SRPAC are spectroscopies in the time domain. NFS, as a coherent scattering process, gives access to the splitting of all nuclear levels, ground and excited, due to interference in the time spectra. In contrast SRPAC, as an incoherent single nucleus scattering process, only gives access to the splitting of the intermediate nuclear level, i.e., the excited one.

1.4.1 Absorption

The cases of the SMS and SRMS resemble closely the "classical" Mössbauer spectroscopy (see e.g. [10] and as well in various chapters of this book). Set-up, experimental details as well as the data evaluation are the same as in classical Mössbauer spectroscopy. The only difference is the source with its special properties such as lineshape, 100% linear polarization, and 100% resonant quanta, which is discussed in Sects. 1.3.1 and 1.6.1.3.

1.4.2 Dynamical Beats

For samples with a large effective thickness, $t_{\mathrm{eff}} = n_{\mathrm{MB}}\, d\, \sigma_0\, f_{\mathrm{LM}}$, with n_{MB} the density of Mössbauer nuclei, d the geometrical thickness, σ_0 the resonant Mössbauer cross section, and $\mathrm{f_{LM}}$ the Lamb-Mössbauer factor, a *speed-up* effect is observed and dynamical beats (*Bessel beats*) show up in the time spectra of NFS.

In Fig. 1.8 the situation is shown for Mössbauer and NFS spectra. For a thin sample, $t_{\mathrm{eff}} = 1$, we have a single Lorentzian line in the Mössbauer spectrum, which corresponds to an exponential decay in the NFS spectrum (Fig. 1.8a, b, dotted lines). Increasing the effective thickness ($t_{\mathrm{eff}} = 25$) the Mössbauer line becomes much wider and non-Lorentzian (Fig. 1.8a, solid line). In the NFS spectrum (Fig. 1.8b, solid line) we observe two features: (1) a speed-up, showing up as an acceleration of the initial decay rate accompanied by an increase in intensity at early times (from 10^7 to 10^9 units in the present example) and (2) a dynamical beat structure is superimposed to the decay. From this beat structure the effective thickness and correspondingly f_{LM} can very precisely be determined.

1.4.3 Quantum Beats

As it is well known, hyperfine interactions might shift and split the nuclear levels. This is described by the Hamiltonian $\mathscr{H}$ as:

$$\mathscr{H} = \mathscr{H}_0 + \mathscr{E}_0 + \mathscr{M}_1 + \mathscr{E}_2 + \ldots \tag{1.25}$$

with $\mathscr{H}_0$ representing all terms, which do not include hyperfine interactions and cause no shift or splitting, $\mathscr{E}_0$ the Coulombic interactions, i.e., the electric monopole term (isomer shift), $\mathscr{M}_1$ the magnetic dipole and $\mathscr{E}_2$ the electric quadrupole interaction. A detailed discussion might be found in [10] and will be mentioned in more detail as well in other chapters of this book. In the energy domain such as Mössbauer spectroscopy several absorption lines reveal this splitting whereas in the time domain such as NFS and SRPAC an interference pattern, the quantum beat structure, shows up.

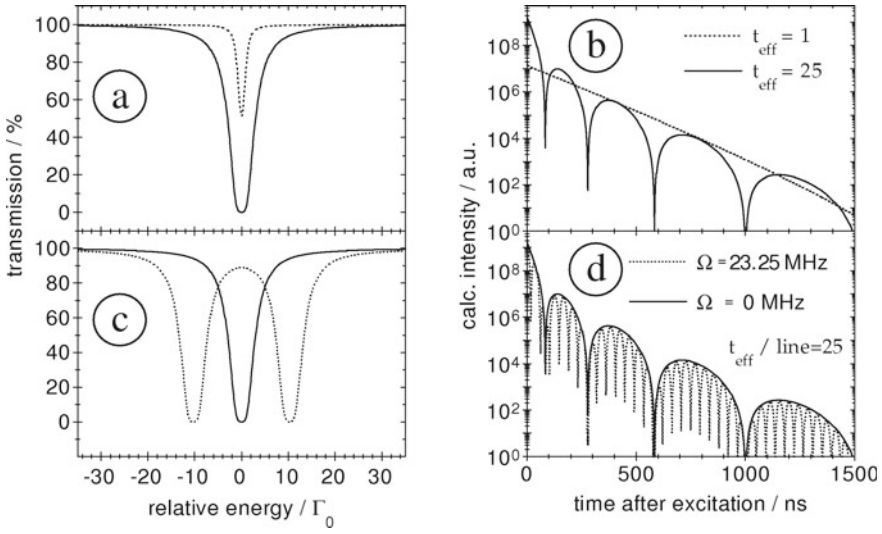

Fig. 1.8 Simulations of corresponding spectra of Mössbauer spectroscopy (left panel, with $\Gamma_0 = \hbar/\tau_0$) and NFS (right panel) for thin ($t_{eff} = 1$) and thick ($t_{eff} = 25$) samples. For the single lines (panel a and b) the thin sample leads to an exponential decay whereas the spectrum from the thick sample is further modulated by the dynamical beats. In panel c the energy spectra of a thick sample ($t_{eff} = 25$) with one (solid line) and two (dotted line) transition lines, respectively, are shown. In panel d the corresponding time spectra are shown. The sample with the two lines shows in addition to the dynamical beats the fast, equidistant quantum beat structure superimposed (from [86])

In case of electric quadrupole interaction ($\mathscr{E}_2$) the excited nuclear state, I = 3/2 in case of ^{57}Fe, splits to the $\pm 3/2$ and $\pm 1/2$ levels. This gives rise to two absorption lines in Mössbauer spectroscopy (see dotted line in Fig. 1.8 c). The corresponding spectrum in NFS shows up as an interference pattern of these two transitions with a single frequency Ω of the quantum beats (see dotted line in Fig. 1.8 d). Due to the thick sample with an effective thickness $t_{\mathrm{eff}} = 25$, the dynamical beat structure is strongly modulating the quantum beats as an envelope. It is clearly seen that the quantum beat structure is equidistantly spaced whereas for the dynamical beat structure the distance of the minima increases with time. This can be described for NFS in a good approximation by

$$I_{\mathrm{NFS}}(t) \propto \frac{t_{\mathrm{eff}}}{t/\tau_0} \cos^2\left(\frac{\Omega t}{2}\right) \cdot \mathrm{e}^{-\frac{t}{\tau_0}} \cdot J_1\left(\sqrt{4 t_{\mathrm{eff}}\, t/\tau_0}\right)^2 \tag{1.26}$$

and for SRPAC by

$$I_{\mathrm{SRPAC}}(t) \propto \mathrm{e}^{-\frac{t}{\tau_0}} \{1 - A_{22} \cos^2\left(\frac{\Omega t}{2}\right)\}. \tag{1.27}$$

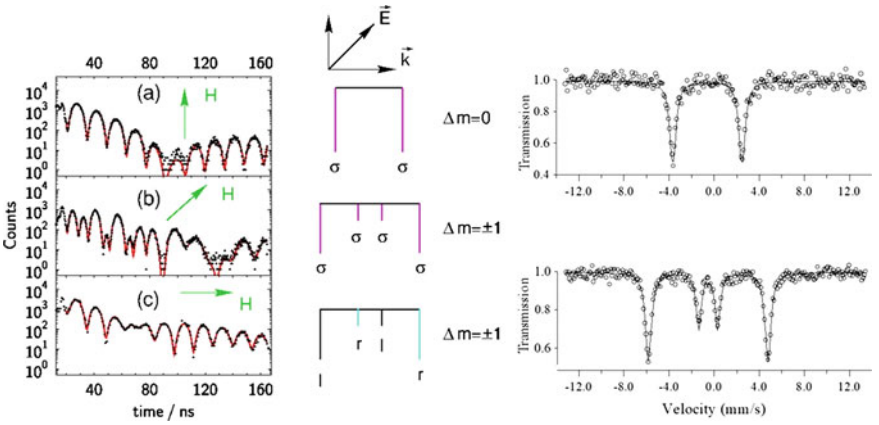

Fig. 1.9 Left panel: measured time spectra of iron (NFS) in case of magnetic hyperfine interaction for various alignments of the hyperfine field **H** with respect to the wave vector **k** and the polarization **E**. Solid lines are fits according to the full theory. middle panel: nuclear transition lines with their polarization state, σ—σ linearly polarized, l and r—left and right hand circular polarized, respectively. Δm - change of magnetic quantum number. (Reprinted by permission from Nature Springer: ref. [87], copyright 2003) right panel: Measured energy spectra of iron (SMS) in case of magnetic hyperfine interaction for various alignments of the hyperfine field **H** with respect to the wave vector **k** and the polarization **E** (note: **E** points now up). For the absorption spectra the two cases for $\Delta m = \pm 1$ are indistinguishable. Solid lines are fits with the transmission integral. (Reprinted figure with permission from [54], Copyright (1997) by the American Physical Society)

The term $\cos^2(\frac{1}{2}\Omega \cdot t)$ describes in both cases the quantum beats. The Bessel function J_1 describes the dynamical beats and A_{22} the anisotropy and angular dependence. For comparison the unsplit case is shown as solid lines in the same figures. Changing the strength of the hyperfine interaction will result in a different splitting and correspondingly in a different quantum beat frequency Ω.

In case of magnetic hyperfine interaction full splitting of the nuclear levels occurs giving rise to six nuclear transitions and correspondingly to six absorption lines in Mössbauer spectroscopy with ^{57}Fe. In NFS spectroscopy a more detailed interference pattern will result. Contrary to conventional Mössbauer spectroscopy where the γ-rays from the radioactive source are normally unpolarized now the x-rays from the synchrotron radiation source and the γ-rays from the SMS are highly linearly polarized. This feature strongly modifies the spectra. Corresponding time and energy spectra are displayed in Fig. 1.9. The important parameters are the orientation of the three vectors with respect to each other, the wave vector **k**, the polarization vector **E**, and the hyperfine field vector **H**.

If all three vectors are perpendicular to each other only the two $\Delta m = 0$ transitions contribute to the spectrum, resulting in a two-line spectrum for the SMS (Fig. 1.9 upper right), and consequently in a simple quantum beat pattern with one single frequency and high contrast (Fig. 1.9 upper left). In case of NFS a similar spectrum with only one frequency, however, with less contrast appears when $\mathbf{H} \parallel \mathbf{k}$. In this case

the two $\Delta m = +1$ and the two $\Delta m = -1$ transitions interfere independently giving now rise to left and right hand circular polarization (Fig. 1.9c). Finally, for $\mathbf{H} \parallel \mathbf{E}$ all $\Delta m = \pm 1$ transitions interfere giving rise to a more complicated spectrum which is sigma polarized (Fig. 1.9b). The slow overall modulation is caused by dynamical beats due to the finite effective thickness. In case of the SMS the two cases with $\Delta m = \pm 1$ transitions are indistinguishable in a simple absorption experiment and the resulting spectra resemble four-line absorption spectra (Fig. 1.9 lower right).

1.5 Structural Dynamics

Structural dynamics is accessible via quasi-elastic scattering techniques in the energy domain by RSMR or directly in the time domain by TDI and NFS/SRPAC measuring translational and rotational dynamics and via inelastic scattering techniques, NIS and IXSNRA, in the energy domain giving access to the phonon density of states.

1.5.1 Quasi-elastic Dynamics

Nuclear quasi-elastic scattering measures structural dynamics on a ps to μs time scale. The coherent and the incoherent channel can be utilized. In the first case, the coherent channel, the Lamb-Mössbauer factor has to be greater than zero ($f_{LM} > 0$). The set-up is the same as in NFS (see Fig. 1.7). The incoming x-ray pulse creates a coherent collective nuclear state which decays in the static case in forward direction. Dynamics, e.g. the jump of a Mössbauer nucleus from one atomic site to another (in space and angle, see e.g. [88]), destroys this state. As a consequence no x-ray is scattered in forward direction, i.e., the measured intensity in the NFS detector is decreased at later times. We will get an 'accelerated decay' or a 'damping' of the NFS intensity $I_{NFS}(t)$, which might be described in a simplified picture by:

$$I(t) \propto I_{\mathrm{NFS}}(t)\, \mathrm{e}^{-2\lambda_t t}\, \mathrm{e}^{-\lambda_r t}. \tag{1.28}$$

The first exponential is related to the van Hove self-intermediate function [89] with λ_t being the translational relaxation rate and the second one to the rotational correlation function with λ_r being the rotational relaxation rate.

In the second case, the incoherent channel, the scattering is independent of the Lamb-Mössbauer factor. The set-up is the same as in SRPAC (see Fig. 1.7). The incoming x-ray pulse selectively excites a single nucleus, which decays in the static case with an angular distribution according to the anisotropy parameter, A_{22}. Dynamics, e.g. rotational motion monitored by the electric hyperfine interaction $\hbar\Omega$, changes this distribution and gives rise to a damping of the intensity signal.

The perturbation factor G_{22} in the scattering intensity I_{SRPAC} (see Eq. 1.24) reduces in the slow approximation to

$$G_{22}(t) \propto \mathrm{e}^{-\lambda_r t} \cos^2\left(\frac{\Omega t}{2}\right) \tag{1.29}$$

and in the fast approximation to

$$G_{22}(t) \propto \mathrm{e}^{-(\Omega^2/\lambda_r)t}. \tag{1.30}$$

Combining both techniques the translational and rotational relaxation rates can be separately extracted.

In both cases described above the sample has to contain the Mössbauer isotope. For samples without Mössbauer isotopes a variant—time domain interferometry [69] or Rayleigh scattering with Mössbauer radiation—may be utilized, see Sect. 1.3.5.

In the default TDI setup [69], with two identical single line resonance absorbers, the interference of the probe and reference waves is described by

$$I(\mathbf{q}, t) \propto I_{\mathrm{NFS}}(t)(1 + f_{qe}(\mathbf{q}) \cdot \cos \Omega t \cdot S^n(\mathbf{q}, t)), \tag{1.31}$$

where $I_{\mathrm{NFS}}(t)$ is the single line response of the two resonance absorbers, Ω is the frequency difference in the response of the two absorbers, $f_{eq}(\mathbf{q})$ is the elastic (including the quasi-elastic part) fraction of scattering, and $S^n(\mathbf{q}, t)$ is the normalized intermediate scattering function, i.e., the normalized Fourier transform of the dynamic structure factor.

As described by Eq. 1.31 the TDI pattern displays an oscillating dependence, where an envelope of the fading contrast is given by the intermediate scattering function.

For more details on the TDI technique see in this book Seto et al. [60].

1.5.2 Phonon Density of States

Nuclear inelastic scattering measures the *(partial) phonon density of states* of the Mössbauer element in the sample. As an example the intensity of nuclear inelastic scattering of synchrotron radiation in a polycrystalline α-iron sample at room temperature is shown as a function of energy of the incident radiation (Fig. 1.10).

The central peak corresponds to elastic scattering. The structure beyond the central peak shows the energy dependence of inelastic scattering (furtheron called "energy spectrum"), accompanied either by creation ($E > 0$) or by annihilation ($E < 0$) of phonons. At ambient temperature one may recognize various contributions to the energy spectrum, which correspond to inelastic scattering accompanied by creation or annihilation of a different number of phonons.

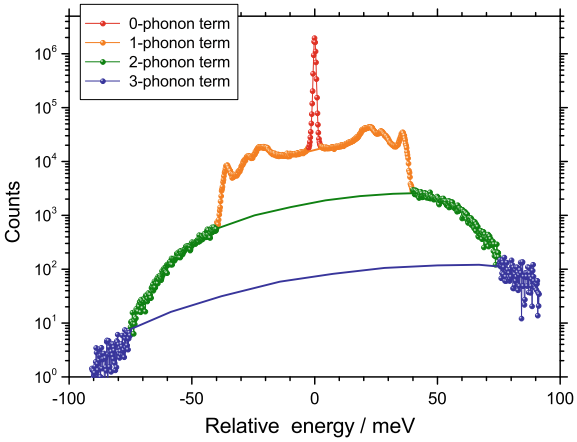

Fig. 1.10 Expansion of the energy spectrum of nuclear inelastic scattering of synchrotron radiation in α-iron in multi-phonon terms. The data were taken at room temperature. Different symbols show the regions of the spectra, where the corresponding contributions are dominant. The lines are the calculations according to Eqs. 1.32–1.34 and convoluted with the instrumental function of the monochromator

The normalized probability of nuclear inelastic scattering $W(E)$ can be decomposed in terms of a multiphonon expansion [90]

$$W(E) = f_{\mathrm{LM}} \left(\delta(E) + \sum_{n=1}^{\infty} S_n(E) \right). \tag{1.32}$$

The Dirac δ-function $\delta(E)$ describes the elastic part of scattering (zero-phonon term), and the n-th term of the series $S_n(E)$ represents the inelastic scattering accompanied by creation (annihilation) of n phonons. The one-phonon term is given by

$$S_1(E) = \frac{E_R \cdot g(|E|)}{E(1 - \mathrm{e}^{-\beta E})}, \tag{1.33}$$

and the subsequent terms under harmonic approximation may be found through the recursive relation:

$$S_n(E) = \frac{1}{n} \int_{-\infty}^{\infty} S_1(E') \cdot S_{n-1}(E - E')\, \mathrm{d}E'. \tag{1.34}$$

Here $\beta = (k_{\mathrm{B}} T)^{-1}$ with k_{B} the Boltzmann constant, T the temperature; $E_{\mathrm{R}} = \hbar^2 k^2 / 2M$ the recoil energy of a free nucleus; k the wave vector of the x-ray quantum; M the mass of the atom. The function $g(E)$ is the normalized phonon density of states

$$g(E) = V_0 \frac{1}{(2\pi)^3} \sum_j \int \mathrm{d}\mathbf{q}\ \delta\left[E - \hbar\omega_j(\mathbf{q})\right], \tag{1.35}$$

where V_0 is the volume of unit cell, index j numerates the branches of the dispersion relation $\hbar\omega_j(\mathbf{q})$, $\mathbf{q}$ is the phonon momentum, and the integral is taken within the first Brillouin zone. The detailed theory of nuclear inelastic scattering has been published by several authors [90–92].

Using the sum rules [93, 94], from the nuclear inelastic scattering spectra and from the phonon density of states other (thermo) dynamic quantities can be derived such as the Lamb-Mössbauer factor, the mean square displacement, the mean kinetic energy, the mean force constant, the mean force, and the second order Doppler shift. In addition, from the density of states the lattice specific heat at constant volume and pressure, and the vibrational entropy can be determined.

In summary, NIS gives direct access to the partial phonon density of states and various (thermo) dynamic quantities. It is complementary to methods as inelastic neutron, x-ray, and light scattering. In those techniques mainly dispersion relations are measured, which are fitted to a model and in a final step the phonon density of states can be derived. For more details see Seto et al. [60].

As mentioned above, IXSNRA measures an "x-ray generalized" phonon density of states. The data evaluation procedure is along the same route as for NIS outlined above. In the data treatment, the x-ray generalized phonon density of states can be reduced to the true phonon density of states using a so-called "correction function", when it is available from theory or computer simulation [95].

1.6 Experimental Details

NRS relies very much on the outstanding brilliance and timing properties of 3rd generation synchrotron radiation sources such as APS, ESRF, PETRA III, and SPring-8. Dedicated insertion devices, perfect high-resolution and focusing/collimating x-ray optics, and fast detector systems assure optimal conditions for NRS applications.

As an example the layout of the Nuclear Resonance beamline at the ESRF is shown in Fig. 1.11. The undulators define the maximum available photon flux. One set of the magnet structures, U20, is optimized for 14.4 keV, the resonance energy of the most utilized MB isotope, ^{57}Fe, and the other magnet structure (U27) for the transition energies of other MB isotopes starting with 21.5 keV (^{151}Eu). The first optics hutch (OH1) contains the cryogenically cooled high-heat-load mocnochromator (6–80 keV). The second optics hutch (OH2) contains all high-resolution optical elements. Three experimental hutches are available to the users for their experiments.

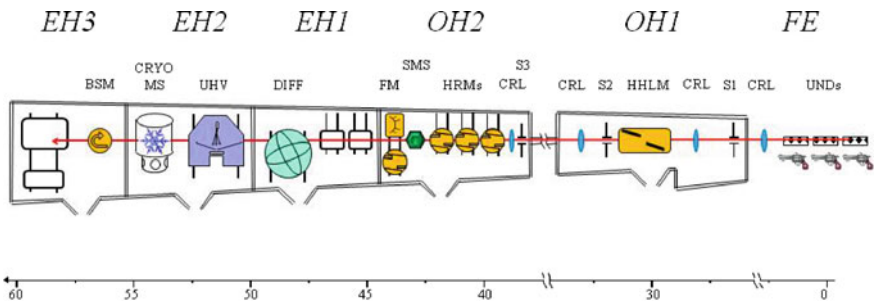

Fig. 1.11 Schematic layout of the nuclear resonance beamline (ID 18) at the ESRF. FE—front end; UNDs—three revolver type undulators with periods λ_u of 20 and 27 mm; OH1, OH2—optics hutches, EH1, EH2, and EH3—experimental hutches, CRL—focusing and collimating compound refractive lenses, S1, S2, and S3—slit systems, HHLM—Si(111) high heat-load monochromator, HRMs—high-resolution monochromators, SMS—synchrotron Mössbauer source, FM—focusing monochromator, DIFF—DIFFractometer, UHV—set-up for in-situ preparation, characterization and NRS measurements of surfaces, interfaces, and nano-structures, CRYO—CRYOmagnet system, BSM—backscattering monochromator

1.6.1 X-Ray Optics

Nuclear level widths are in the range of neV to μeV (e.g. 4.66 neV for ^{57}Fe), whereas energy bandwidths of SR from undulators are in the range of 100 eV. That immediately makes clear that dedicated and optimized SR sources and excellent x-ray optics are needed to achieve not only highest brilliance but also highest flux. Nowadays, x-ray optics for NRS applications ranges from eV resolution, via meV resolution, and eventually to neV resolution, i.e., spanning more than eleven orders of magnitude. The needed resolution is on the one side determined by the spectroscopy (e.g. NIS) and on the other side by the demand not to overload the detector system (e.g. NFS).

1.6.1.1 High Resolution Monochromator

For sub-meV resolution, mandatory e.g. for phonon spectroscopy, in-line silicon high-resolution monochromators based on the 'nested design' [96] or the flux-optimized design [97] are common practice. They may be tailored with high efficiency for energies below about 30 keV.

Figure 1.12 left panel displays the nested-design consisting of two channel-cut high-quality Si crystals, which are mounted in a nested geometry. Asymmetric cuts and a proper choice of reflections assure high throughput and fixed and high energy resolution.

The adopted scheme of the flux-optimized HRM is shown in Fig. 1.12 right panel. Actually, at the ESRF, we have implemented, as shown in the figure, two of those HRMs next to each other on one mechanics, each consisting of four flat Si single crystals, which offer 0.5 and 2 meV resolution just by a horizontal translation of the

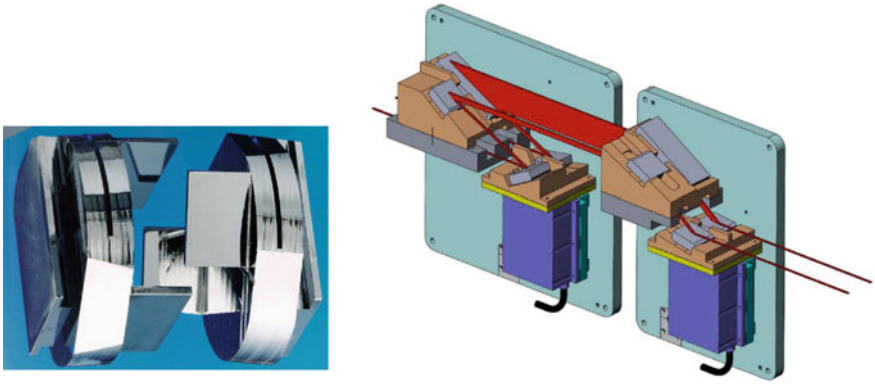

Fig. 1.12 Left panel: nested design of a four-bounce channel-cut HRM. Right panel: double-resolution monochromator with high-energy resolution and optimized intensity: the two first crystals in asymmetric reflections provide in two steps extreme angular collimation of the incident radiation. The two subsequent reflections with the opposite indexes of asymmetry serve as two-step energy analyzer

mechanics. This solution allows especially in NIS for a trade-off between energy resolution and flux.

1.6.1.2 Backscattering Monochromator

For higher energies these silicon HRMs are no longer efficient and backscattering monochromators may be an alternative. The classical approach with a silicon crystal [98] does not work for NRS due to the fixed energies given by the Mössbauer levels. Other materials have to be exploited such as sapphire [21]. However, the needed crystal's quality is still lacking [99].

1.6.1.3 Synchrotron Mössbauer Source

For extreme monochromatization, the SMS provides a fully resonant, polarized, and collimated γ-ray beam with an energy resolution in the neV regime at 14.4 keV [54]. Currently, SMSs are installed at SPring-8 [56] and the ESRF [57] (see Fig. 1.13 as an example at the ESRF). Details of the SMS, theoretical and technical, are laid down in several articles [52, 54, 57, 58, 100–102].

The key element of the SMS is an iron borate $^{57}FeBO_3$ single crystal enriched in the ^{57}Fe isotope up to 95%. Iron borate is a canted antiferromagnet with a Néel temperature of 348.35 K. The crystal is set to electronically forbidden but nuclear allowed [111]- or [333]-reflections to extract the purely scattered nuclear signal. At room temperature $^{57}FeBO_3$ shows in this diffraction geometry with polarized SR a four line spectrum due to hyperfine splitting of the nuclear levels with a flux

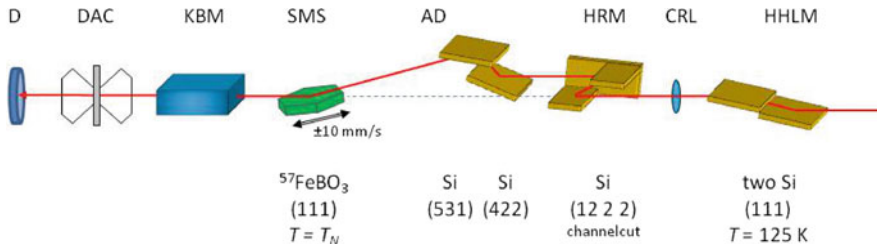

Fig. 1.13 Optical scheme for a high-pressure experiment at the ESRF with the DAC using the SMS based on the $FeBO_3$ (111) pure nuclear reflection. HHLM, high-heat-load monochromator; CRL, compound refractive lens; HRM, Si (12 2 2) high-resolution monochromator; AD, Si (422)—Si(531) angular deflector; SMS, iron borate crystal inside the furnace with magnets and mounted on the Mössbauer transducer and two-circle element; KBM, Kirkpatrick-Baez multilayer mirrors (focusing optics); DAC, diamond anvil cell; D, detector

of about 10^6 photons/s. However, a special case of combined magnetic dipole and electric quadrupole interactions can be realised close to its Néel temperature in the presence of a weak external magnetic field, where a single-line spectrum of the emitted radiation can be obtained. The energy width of the emitted line is close to the natural width of the Mössbauer resonance (see Eq. 1.23). It is very sensitive to the temperature and magnetic field applied across the crystal. Therefore, the temperature of the borate crystal has to be stabilized with milli-Kelvin accuracy. Depending on the exact temperature the linewidth may be chosen according the experimental needs. However, narrower linewidths correlate with lower flux. For example, for a linewidth of $3\,\Gamma_0$ the flux is about $2\,10^4$ photons/s whereas, for a linewidth of $2\,\Gamma_0$ it is about 10^4 photons/s. The energy variation of the γ-ray beam is achieved as in classical MB spectroscopy by Doppler shift of the "source", i.e., in this case the borate crystal. Due to technical issues it is done by a sinusoidal acceleration.

The heat-load of the incoming x-ray beam on the crystal is reduced by the upstream HRM. Further, the angular deflector (AD, see Fig. 1.13) together with the borate crystal keeps the γ-ray beam horizontal.

Furthermore, as discussed in Sect. 1.3.1, the $^{57}FeBO_3$ crystal rotates the sigma polarization by 90°, i.e., the γ-ray beam is π-polarized. Other polarization options may be achieved with phase plates [103].

1.6.1.4 Focusing

A big asset in nuclear resonance techniques compared to classical MB spectroscopy are the focusing capabilities of the radiation. Several options may be employed such as bent monochromators [104], KB-optics [105], compound refractive lenses (CRL) [106], and Fresnel zone plates (FZP) [107]. A general requirement to focusing optics for nuclear resonance applications is that it has to keep the high spectral flux, i.e., to accept the entire SR beam. In case of bulky sample environment

such as cryo-magnet or UHV systems a rather large focal distance (∼1 m) is an asset. The best trade-off is achieved with graded multilayer optics in Kirkpatrick-Baez geometry [108]. At the Nuclear Resonance beamline at the ESRF a spot size of about $5 \times 10\,\mu m^2$ (v × h) at 1 m focal distance and with high flux is available.

1.6.2 Detectors

For nuclear resonance scattering experiments detectors with (sub-) ns time resolution, high dynamical range, and fast recovery time are mandatory. Beam intensities of 10^9 photons/s in the prompt pulse (i.e. 200 photons per bunch in 16-bunch mode at the ESRF) are common conditions. The detector must survive this intense prompt flash and be able to count few nanoseconds later a single photon event of the delayed nuclear radiation. State-of-the-art detectors are nowadays avalanche photo diode (APD) detectors [109, 110].

The performance can be summarized as:

- dynamic range and linearity is assured over nine decades of intensity
- efficiency: 40% at 14.4 keV
- background: 0.02 photon/s
- time resolution 100 ps to about 1 ns.

Depending on applications and energy regime stacked (up to 24) and inclined detectors are common practice in order to improve the efficiency.

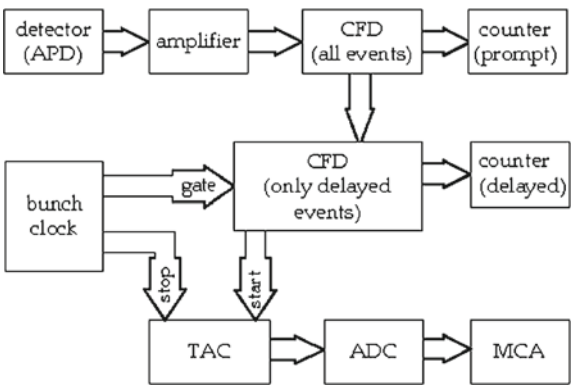

Fig. 1.14 Timing electronics for NRS experiments: it allows one to count both all events, which are pratically the overhelming charge scattered events, and the *delayed* nuclear scattered events. The time spectra are recorded with a MCA. CFD—constant fraction discriminator, TAC—time-to-amplitude converter, ADC—analog-to-digital converter, MCA—multichannel analyzer, bunch clock—reference rf-signals from the SR source

Time spectra are collected in the traditional 'start-stop' technique (see Fig. 1.14). Normally, the detector signal is the "start" signal whereas the "stop" signal is derived from the bunch clock, i.e., the reference signal of the rf-frequency of the SR source.

Fast time-to-digital converter and digitizer techniques are under development in order to improve (i) the response time at early times (< 5 ns) needed especially for Mössbauer isotopes with short life times, (ii) the throughput, and (iii) to allow for "multi-hit" operation. The multi-hit option together with high throughput avoids time gating of the prompt pulse and is mandatory for experiments at the new XFEL sources [111]. Furthermore, fast position sensitive detectors [112–114] received attention for applications such as NSAS, TDI, SRMS.

1.6.2.1 Resonance Detector

For some applications such as IXSNRA, SRMS, and RSMR the energy analysis is carried out with a so-called resonance detector. In principle it consits of an x-ray detector like an APD with its timing electronics and an absorber or a scatterer, which contains the Mössbauer isotope for the resonance analysis.

In the simplest case like IXSNRA the APD is covered e.g. by an $\alpha-{}^{57}$Fe foil. When the energy of the incident radiation matches the energy of the nuclear transition, the scattering leads to nuclear forward scattering in the foil of the resonance isotope. By time discrimination only the (delayed) NFS signal of the time spectrum is taken and time integrated. This resulting signal measures only "resonant quanta" and is used for the energy analysis.

For SRMS the details of the detector system are more sophisticated and will be described in detail in this book by Seto et al. [60]. In case of RSMR (and the SMS) normally time discrimination is not necessary due to the "100%" resonant beam.

1.6.3 Sample Environment

Versatile sample environment is a prerequisite for a holistic approach of the investigation of novel systems. Nuclear resonance techniques by themselves may contribute in the study of electric, magnetic, and structural properties, static and dynamic. Combining those techniques with other on-line and off-line techniques such as XRD, MOKE, transport measurements, etc., will foster a holistic picture. Especially the small beam size and divergence of synchrotron radiation favours sophisticated experimental environments not feasible in the home laboratories with radioactive sources. Standard equipment allows for applying e.g. a combination of low temperature, high pressure, and high magnetic field. Other examples are UHV systems for in situ investigation of surface, interfaces, and nano-structured materials [115]; laser heating system combined with high pressure for in situ investigation of the Earth's interior and new materials [116]; pulsed high-magnetic field [117]; combined RAMAN and IR environment for the investigation of cross-over systems and protein dynamics [118].

1.7 Applications

In this chapter, on the basis of recent applications and developments of NRS at the Nuclear Resonance beamline at the ESRF, we attempt to foresee future applications of NRS, focusing on most challenging scientific cases. Driven by the expected instrumental development of Nuclear Resonance Scattering at Extremely Brilliant Source (EBS) at the ESRF, we analyse possible future applications in two conceptual frames: *Nano-Scale Science* and *Micro-eV Atomic Dynamics*.

1.7.1 Nano-Scale Science

With the EBS Upgrade Programme [119], the Nuclear Resonance beamline at the ESRF expects to offer users with the beam size of about 200 nm. This development is expected to be most beneficial for studies at ultra-high pressure and in fields such as magnetism, superconductivity, geoscience, and nano-paleomagnetism.

1.7.1.1 Ultra-High Pressure

High-pressure studies are one of the evident highlights of nuclear resonance scattering experiments with synchroton radiation sources. This is driven by the intrinsic small size and collimation of synchrotron radiation and by the straightforward focusing capabilities using compound refractive lenses and Kirkpatrick-Baez optics, respectively.

At present, the available beam size at nuclear resonance beamlines is about 10 μm. This is sufficient to use most elaborated single-stage diamond anvil cells (DACs), allowing to reach pressures as high as a few hundreds GPa. Figure 1.15 outlines the studies of magnetism in Ni metal, conducted at pressures up to 260 GPa [120]. Though the statistical accuracy of the data at highest pressures is relatively moderate, it nevertheless enables the reliable determination of the magnetic hyperfine field. The data provide a solid evidence that Ni stays ferromagnetic up to 260 GPa, the highest pressure where magnetism has been observed so far (Fig. 1.15, left panel). They also reveal the importance of accounting for relativistic effects in the theory of magnetic interactions in Ni (Fig. 1.15, right panel).

The above example showcases the frontiers of high-pressure research at existing nuclear resonance beamlines. However, they are still far away from the limits of available static-pressure equipment, determined by recently developed double-stage diamond anvil cells [121].

In the double-stage DAC, a sample is pressurized between two micro-anvils (semi-balls made of nanocrystalline diamonds), which are attached to the culets of the opposed gem quality diamonds (Fig. 1.16). Due to the small diameter of the

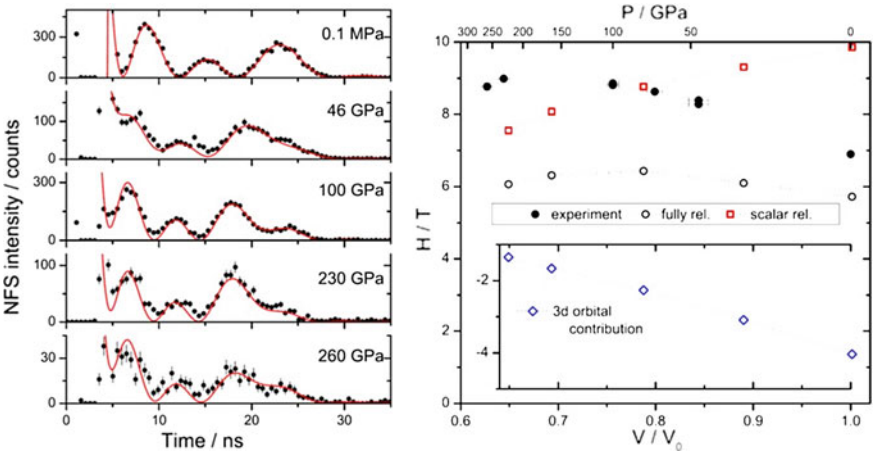

Fig. 1.15 Left: time evolution of nuclear forward scattering for Ni at various pressures. The *(red) solid lines* show the fit. The period of oscillations of the signal is inversely proportional to the magnetic hyperfine splitting. Right: pressure dependence of the magnetic hyperfine field in Ni from the experiment (*solid black circles*) and from fully relativistic ab initio calculations (*open black circles*). Positive and negative contributions to the calculated field are shown as scalar relativistic calculations (*red open squares*) and 3d orbital contribution (*blue open diamonds*). (Reprinted figure with permission from [120], Copyright (2013) by the American Physical Society)

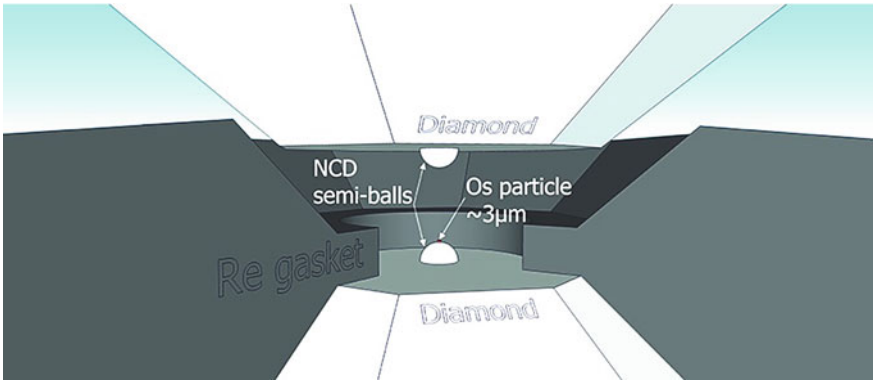

Fig. 1.16 The double-stage diamond anvil cell for ultra-high pressure generation. Semi-balls made of nanocrystalline diamond (NCD) of extraordinary strength are attached to the culets of the opposed gem quality diamonds of the DAC. A sample of osmium (Os), shown as a small red dot on the top of the lower semi-ball, has a size of ca. 3 microns [122] (Image courtesy Elena Bykova, University of Bayreuth)

micro-anvils (10–50 μm), the static pressure limits of these cells approach the TPa range [122].

The typical size of samples in the double-stage DAC is about few microns (Fig. 1.16). In order to study a system under reasonably homogeneous-pressure conditions, the size of the synchrotron radiation beam should be on the (sub-) micron scale. This is not yet available at present nuclear resonance beamlines, but should be enabled by coming Extremely Brilliant Sources of synchrotron radiation.

Furthermore, the sub-micron beam size will greatly improve the quality of high-pressure and high-temperature experiments with laser heating, allowing one to focus the probe beam on the centre of the most heated spot of the sample. With such a beam, the available pressure and temperature range will entirely cover the conditions of the Earth interior, and will open access to studies of matter under conditions of Super-Earth planets interiors.

1.7.1.2 Magnetism

The intrinsic sensitivity of Nuclear Resonance Scattering to the value and direction of magnetic hyperfine fields, combined with a small beam size, allows for imaging of magnetic structures. One of the most impressive example of such studies is the imaging of the spin structure of a magnetic spring [123].

Utilizing the probe layer technique, i.e., inserting ^{57}Fe in various depths of the thin iron film (see Fig. 1.17 right panel), NRS directly probes the actual spin structure in various depths by selectively exciting the ^{57}Fe layer at various lateral positions. The sample investigated here is a bilayer system consisting of 11 nm Fe on 30 nm $Fe_{55}Pt_{45}$ in the hard-magnetic tetragonal $L1_0$ phase. A wedge-shaped 0.7 nm thick ^{57}Fe film with a slope of 0.5 nm/mm has been produced. Different depths D in the sample can thus be probed by adjusting the displacement Δx of the sample transversely to the incident beam [123]. Evaluation of the spectra reveals the depth dependence of the rotation of the magnetization in the iron film with atomic resolution (Fig. 1.17 left panel).

Improving the beam size to the sub-micron scale will enable magnetic imaging of more numerous systems like magnetic domains and domain walls, vortexes, skyrmions, etc. In this sense, the abilities of nuclear resonance scattering will approach the resolution of magnetic imaging with tunnelling microscopy (Fig. 1.18), with the additional option of imaging the chemical and oxidation states of systems. Furthermore, this approach will enable imaging under external stimuli such as extreme temperature and pressure conditions and external electric/magnetic fields and give access to burried and interface layers, not easily accessible by other methods.

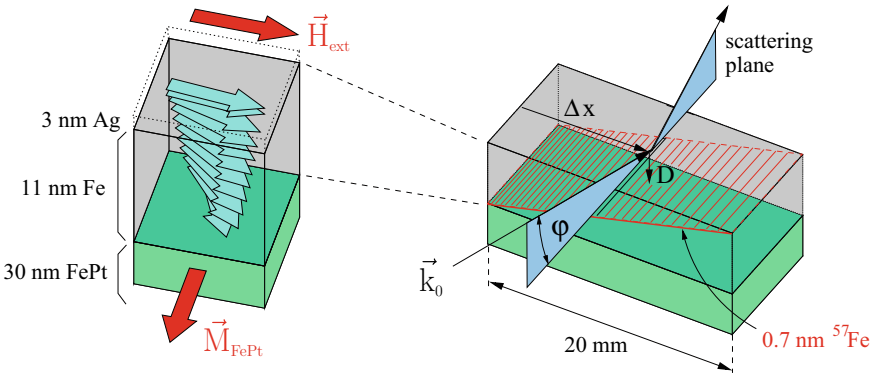

Fig. 1.17 Right panel: scattering geometry of the sample (11 nm Fe on FePt). The incoming x-ray beam with wavevector $\mathbf{k_0}$ impinges the sample at a lateral position Δx probing the spin structure via the wedge-shaped ^{57}Fe probe layer (0.7 nm) at depth D. Left panel: image of the derived spin structure (blue arrows) of the iron layer (image courtesy R. Röhlsberger, Desy, 2002)

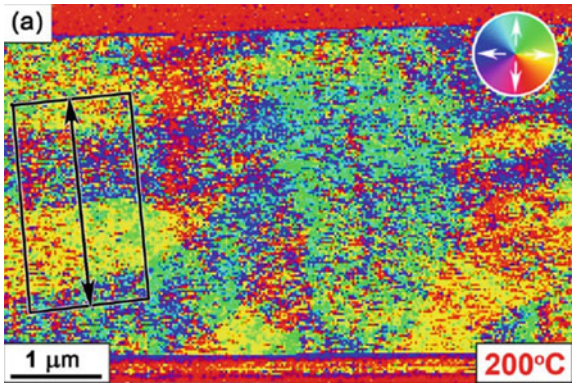

Fig. 1.18 Differential phase contrast magnetic imaging of the planar FeRh thin films. The direction of magnetisation is depicted in the colour wheels (inset). Reprinted through Creative Commons CC BY licence: Ref. [124], copyright 2017

1.7.1.3 Superconductivity

Nuclear resonance scattering provides an elegant and general way to study superconductivity using the Meissner-Ochsenfeld effect [125]. Similar to other applications, this allows one to deal with superconductivity at extreme conditions, which is not easily accessible with standard methods.

A non-magnetic Mössbauer probe is placed inside a sample, which becomes a superconductor (Fig. 1.19). When the NFS spectrum is measured without external magnetic field, one gets a simple exponential decay from a non-magnetic sample. By applying an external magnetic field a splitting of the nuclear levels will appear and, consequently, will cause a quantum beat structure in the NFS spectrum with frequencies corresponding to the strength of the external field [126].

If now the sample is cooled below the critical temperature T_c, the sample becomes superconducting, and the magnetic field is expelled from the sample (Fig. 1.19). Then

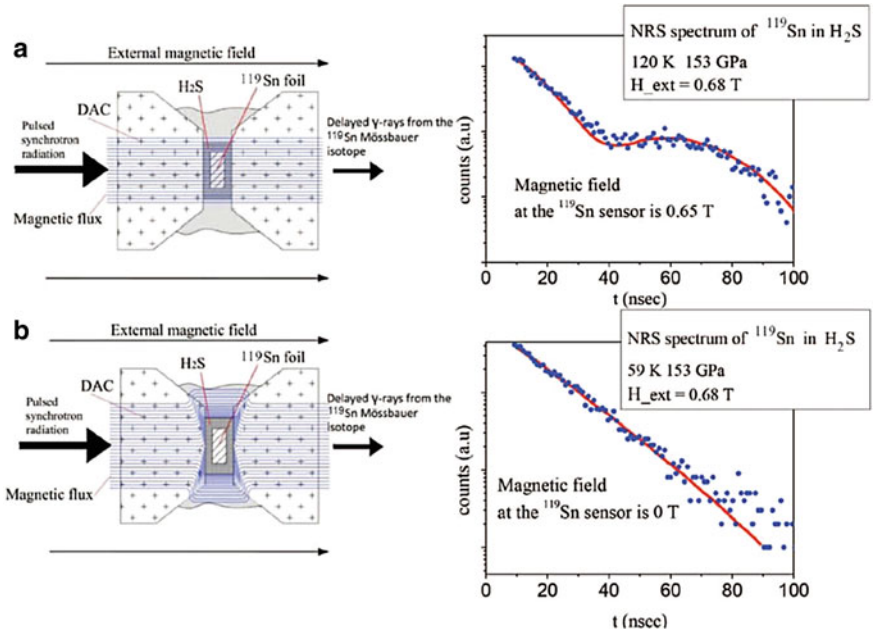

Fig. 1.19 Tin foil, surrounded by compressed H_2S, is located in a DAC at a pressure of about 153 GPa. Synchrotron radiation excites the nuclei of the Mössbauer isotope ^{119}Sn. **a** At high temperature, nuclear forward scattering shows quantum beats due to magnetic splitting of the nuclear levels. **b** At temperatures below the superconducting transition in H_2S, the tin foil is screened from the external magnetic field and, consequently, there is no splitting of the nuclear levels and no magnetic quantum beats in the time spectrum (From [126]. Reprinted with permission from AAAS)

the Mössbauer probe does no longer experience the field and one will again get a simple exponential decay.

In essence, this approach is an alternative to conventional monitoring superconductivity in measurements of magnetic susceptibility with SQUIDs. Instead of putting a sample inside a SQUID, here a small sensor is placed inside a sample. The feasibility of this approach is allowed by the small, micron-scale, size of the synchrotron radiation beam [126].

A further reduction of the beam size to the sub-micron scale will open wide perspectives to study spatial details of superconducting transitions and to image the structures of vortexes and superconducting lamellas. It is well established that the disappearance of a superconducting state proceeds in a spatially-inhomogeneous manner, with creation of an elaborated relief of avalanches of conducting domains penetrating into the residual islands of superconductivity (Fig. 1.20). Studies of the temperature and external field evolutions of these structures at extreme pressure is the next challenge for Nuclear Resonance Scattering.

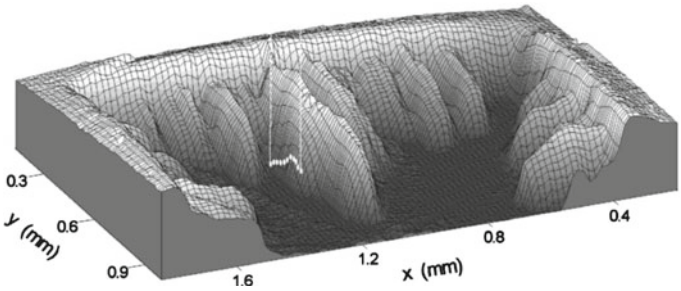

Fig. 1.20 Magnetic landscape in a Nb foil where an array of micro Hall probes (white dots) detect avalanches coming down the slope of the largest flux ridge. The intensity along the vertical axis is proportional to the magnetic field inside the sample (Reprinted figure with permission from [127], Copyright (2004) by the American Physical Society)

1.7.1.4 Nano-imaging

Besides its sensitivity to magnetic structures, nuclear resonance scattering is an established tool to monitor chemical and oxidation states of solids. This enables imaging of chemical and valence structures in real space.

In imaging chemical and oxidation profiles, the mission of nuclear resonance beamlines is to study systems with highly complex micro-size spatial composition. One of the most challenging scientific cases in this aspect are studies of meteorites. Meteorites are slowly cooled (2–9 K per million years) systems, most often consisting of olivine crystals in an Fe-Ni matrix originating from the mantle of a 200-km-radius asteroid [129]. They carry the time-resolved geological, thermal, and magnetic history of the Universe. One of the most intriguing items of these systems is the so-called cloudy zone (CZ), a nanoscale intergrowth of tetrataenite (ordered FeNi) islands of 10–200 nm in size embedded in an Fe-rich matrix, which reveals the time-series record of magnetic activity on an asteroid body. With the current available 10 μm spatial resolution in SMS spectroscopy our understanding of meteoritic metal could already be improved by allowing the cloudy zone to be measured separately from the surrounding metal phases [128]. Scanning along the line crossing the cloudy zone (Fig. 1.21, left panel) is accompanied by drastic changes of the measured Mössbauer spectra, developing from schreibersite to kamacite and further to plessite contributions (Fig. 1.21, right panel). The available 10 μm spatial resolution reveals that the plessite region, previously considered to be a pure-chemical state, actually contains an essential contribution of antitaenite. This finding indicates that the saturation of magnetization in this regions occurs at much lower temperatures than previously thought [128].

However, the most intriguing knowledge on the magnetic history of the Universe is stored in the fine structure of the cloudy zone (Fig. 1.22). The age of the cloudy zone decreases with the distance from the tetrataenite rim [129]. Thus, performing nano-scale imaging of the magnetic, chemical, and coordination states of the

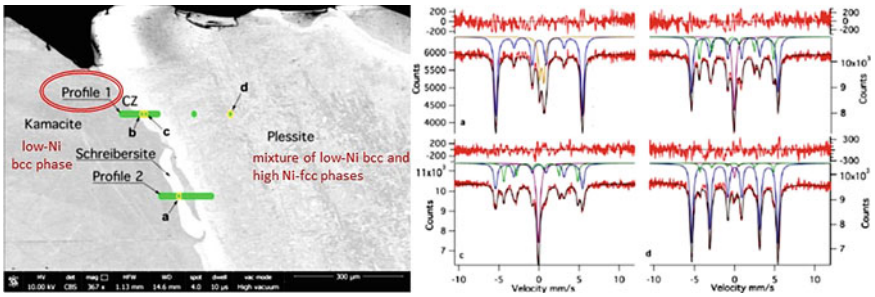

Fig. 1.21 Let panel: scanning electron microscopy image of the Esquel meteorite sample. Green bars mark areas where spectra were obtained. Yellow ovals mark sites where spectra shown on right panel were taken. The size of the ovals represents the size of the beam. Right panel: A selection of representative Mössbauer spectra from the Esquel meteorite: **a** spectrum containing schreibersite; **b** spectrum acquired in the coarse cloudy zone (CZ), closer to the large kamacite lamella; **c** spectrum acquired in the fine cloudy zone, closer to plessite; and **d** spectrum acquired deep into plessite. Reprinted through Creative Commons CC BY 4.0 licence: [128], copyright 2017

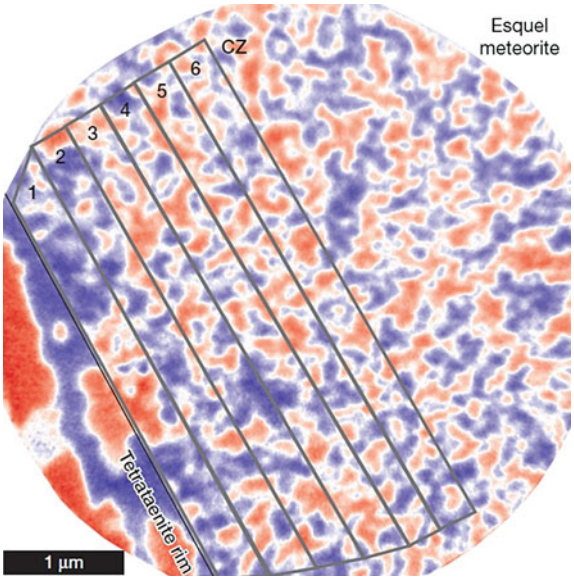

Fig. 1.22 Representative X-ray photoemission electron microscope image of the kamacite, tetrataenite rim and cloudy one (CZ) in the Esquel pallasites. Blue and red colours correspond to positive and negative projections of the magnetization along the X-ray beam direction in the meteorite. The CZ displays a complex interlocking pattern of positive and negative domains. The age of the CZ decreases with distance from the tetrataenite rim. (Reprinted by permission from Nature Springer: [129], copyright 2015)

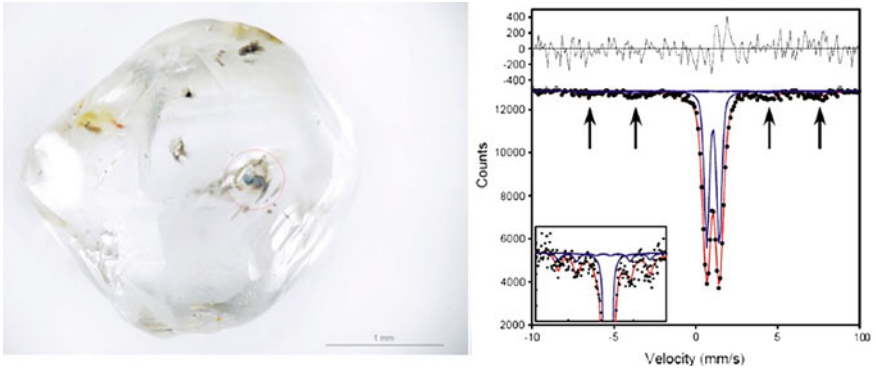

Fig. 1.23 Left: diamond containing ferropericlase inclusion AZ2. Right: Mössbauer spectrum of the inclusion. Solid circles: experimental data; red line: full transmission integral fit assuming one quadrupole doublet and one magnetic sextet. The arrows indicate the positions of four peaks of the magnetic sextet, which can be seen more clearly in the inset that shows a magnified view near the baseline (Reprinted from [130]. Copyright (2016), with permission from Elsevier)

cloudy zone will allow one to recover magnetic, temperature, and thermodynamic conditions of slowly cooled asteroid bodies in their million-years traveling through the Universe. This is what will be possible in nuclear resonance scattering with the expected improvement of the spatial resolution to 100–200 nm.

Another challenging system for nano-imaging of magnetic, chemical, and oxidation states with nuclear resonance techniques are iron-bearing inclusions in diamonds. Syngenetic mineral inclusions in diamonds are pristine witnesses of the chemical and mineralogical environment during diamond formation and thus represent a direct window into the Earth interior. They were for a long period the only source to get information about the interior of the Earth such as the spin and valence states, and the Fe^{3+}/Fe_{tot} ratio of its constituents. Still nowadays they are the only source to get any material at hand from the interior [130].

Already with the presently available resolution of about 10 μm, one can perform spatially-resolved studies of the biggest inclusions. Figure 1.23 shows an example of an iron-bearing inclusion with the size of $192 \times 85 \times 105\,\mu m^3$ (left panel) and the Mössbauer spectrum of one of the parts of the inclusion (right panel), where the presence of a magnetic state is indicated [130].

The expected improvement of the spatial resolution to 100–200 nm will allow for more detailed mapping of the iron-bearing inclusions. Such investigations of the neighbour co-existing chemical phases will enable accessing a wealth of thermodinamical properties of formation of these systems.

Furthermore, the smaller beam size will enable investigations of much smaller inclusions, which accounts for about 95% of the available samples. This will for the first time allow for statistically representative studies.

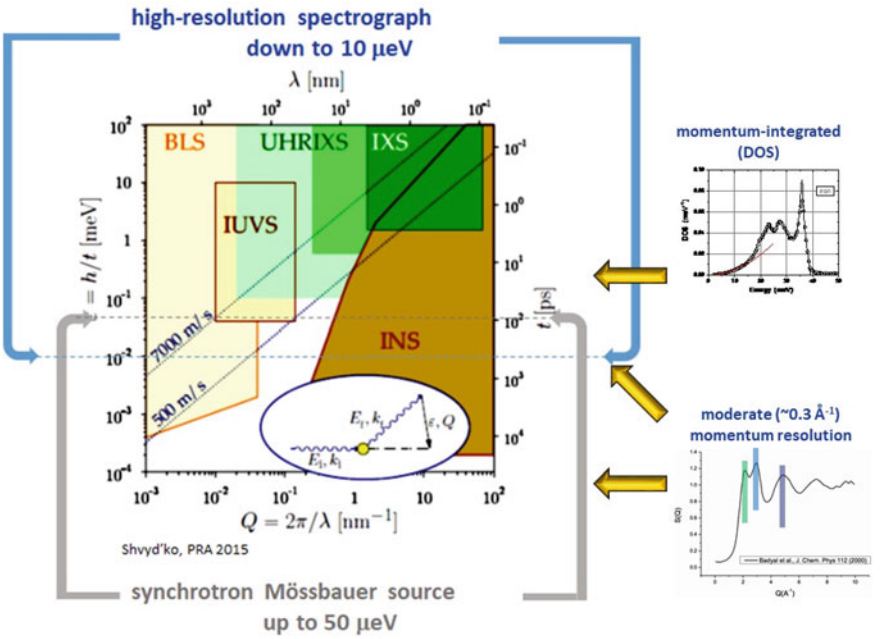

Fig. 1.24 Left panel: Energy-momentum (ε-Q) and relevant time-length (t-λ) space of excitations in condensed matter and how it is accessed by different inelastic scattering probes. The Extremely Brilliant Source Upgrade Programme suggests to improve the energy resolution to about 50 μeV. In addition, the Synchrotron Mössbauer Source available at the Nuclear Resonance beamline at ESRF will allow for scattering experiments with an energy transfer from 1 neV up to 50 μeV for either momentum integrated or moderate momentum resolution conditions (right panels). This will allow one to cover the ~ neV to ~ meV energy range entirely. (Reprinted left figure with permission from [131], Copyright (2015) by the American Physical Society)

1.7.2 Micro-eV Atomic Dynamics

With the Extremely Brilliant Source Upgrade Programme, the Nuclear Resonance beamline at the ESRF expects to offer users with the energy resolution of about 50 μeV. This development will be possibly most beneficial for soft atomic dynamics, geoscience, and glass physics.

1.7.2.1 No-Man's-Land

Figure 1.24 (left panel) shows how the energy-momentum space (or the relevant time-length space) of excitations in condensed matter is accessed by different inelastic scattering probes such as neutrons (INS), x-rays (IXS), ultra-high-resolution IXS (UHRIXS) [131], and photons (ultraviolet (IUVS) and Brillouin (BLS)). It also shows the remaining gap, not accessible by any technique. The expected improvement in

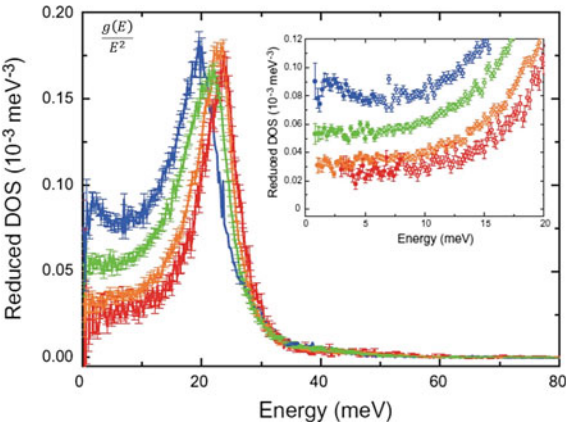

Fig. 1.25 Iron partial reduced phonon density of states (DOS) for four samples of ferropericlase. The inset shows an enlarged reduced DOS (Reprinted from [132] Copyright (2014), with permission from Elsevier)

the energy resolution to about 50 μeV is supposed to close the gap and thereby to enhance capabilities of x-ray techniques.

In addition to the proposed closing of the remaining gap in the energy transfer region from above, we also anticipate to close the gap from below. In particular, the Synchrotron Mössbauer Source available at the Nuclear Resonance beamline at ESRF allows for scattering experiments with an energy transfer from 1 neV to 10 μeV. With an upgraded setup, we plan to reach the energy transfer up to 50 μeV. Thus, both instruments together allow one to cover entirely the ∼neV to ∼meV energy regime.

Even though the proposed development is related either to momentum-integrated studies (DOS) (right top panel) or to measurements with only a moderate momentum resolution ($0.3\,\text{Å}^{-1}$) (right bottom panel), this can be clearly qualified as entering no-man's-land, which will not only help to solve known scientific questions but also will inevitably lead to new fascinating discoveries in fields of geoscience and glass physics.

1.7.2.2 Geoscience

Inelastic x-ray scattering and nuclear inelastic scattering are nearly the only tools to access sound velocity data at extreme conditions such as high pressure and high temperature. While these measurements are relatively easy for model samples, they become progressively complicated for systems with large unit cells and lower mean sound velocities, because the Debye-like parabolic approximation of the DOS is then only valid for much lower energies.

For example, for some samples of ferropericlase [132], a proper determination of sound velocities can be achieved within the energy range below 5 meV (Fig. 1.25, red, orange, and green curves), whereas for other samples this requires precise measurements of the DOS well below 1 meV (Fig. 1.25, blue curve).

Other geophysically meaningful systems like perovskites and wustite require even better energy resolution. Therefore, an achievement of 50 μeV resolution will

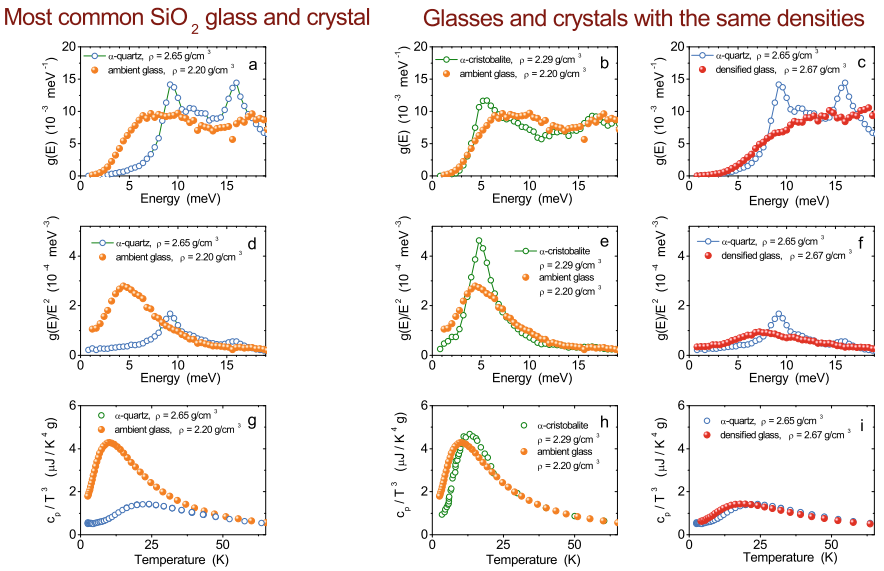

Fig. 1.26 The phonon density of states $g(E)$ (**a**–**c**), the reduced density of states $g(E)/E^2$ (**d**–**f**), and the heat capacity c_P/T^3 (**g**–**i**) for various glassy and crystalline polymorphs of SiO_2. The left panels (**a**, **d**, **g**) compare the most common glassy and crystalline polymorphs and reveal a noticeable difference in the displayed properties. The middle and the right panels compare the glassy and crystalline polymorphs with matched densities, namely, the low-density (**b**, **e**, **h**) and the high-density (**c**, **f**, **i**) polymorphs. They demonstrate that the atomic dynamics and thermodynamics of the glassy and crystalline polymorphs with matched densities do not differ much from each other (Reprinted figure with permission from [95], Copyright (2014) by the American Physical Society)

greatly improve the accuracy of sound velocity measurements, especially for extreme pressure-temperature conditions.

1.7.2.3 Glass Physics

Measurements of the phonon density of states with the presently available energy resolution of about 0.5 meV were already decisive to answer some important scientific questions in glass physics such as the puzzle of the so-called Boson peak (Fig. 1.26). Reliable accessing the atomic dynamics in the 2–5 meV energy range and an ideal integration over the entire range of allowed momentum transfer provide the data, which clearly reveal that the atomic dynamics and thermodynamics of the glassy and crystalline polymorphs with matched densities, contrary to common believes, do not differ much from each other [95].

With the energy resolution improved to about 50 μeV, nuclear resonance scattering may proceed further, to tackle one of the most important scientific cases in glass physics, the nature of the glass transition.

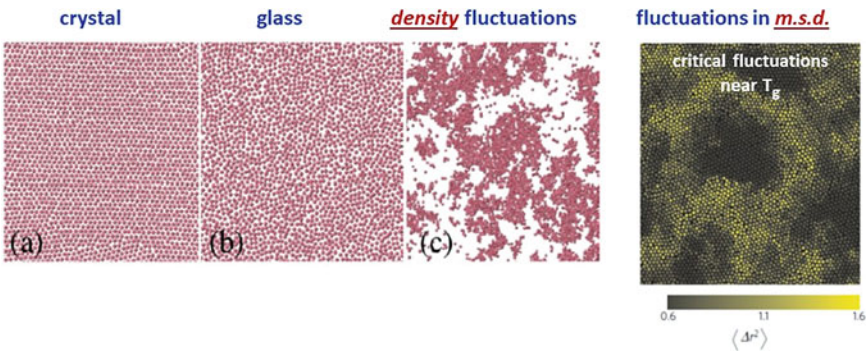

Fig. 1.27 **a** A periodic crystalline structure does not flow because preserving the crystalline order requires moving an extensive set of particles. **b** A mechanically rigid glassy structure exhibits neither the long-range order of a crystal nor the large-scale density fluctuations observed at an ordinary critical point. **c** Large-scale critical density fluctuations near the critical point. (Reprinted figure with permission from [133], Copyright (2011) by the American Physical Society) Right panel: spatial distribution of the mean-square displacement (m.s.d.) of a glass-forming liquid. (Reprinted by permission from Nature Springer: [134], copyright 2010)

Understanding the glass-liquid transition is a challenge, which has resisted the everlasting research efforts of soft condensed matter physics over centuries. Evidence has mounted in recent years that the viscous slowing down of super-cooled liquids might be related to the existence of genuine phase transitions, but of very peculiar nature [133]. One of the most interesting consequences of these ideas is the existence of dynamic heterogeneities (also known as correlated relaxation or correlated diffusion), which have been discovered to be (in the space-time domain) the counterpart of critical fluctuations in standard phase transitions [134].

Dynamic heterogeneity refers to the existence of transient spatial fluctuations in the local dynamical behaviour. The domains of different mobility have no counterpart in the density fluctuations and only appear when dynamics is considered (Fig. 1.27).

Although conceptually of crucial importance, only recently a rather direct evidence for this cooperative motion became available with a suggested cooperative length-scale of about 5–20 molecular diameter at the glass transition [134]. On momentum- and energy-transfer scales, this corresponds to $\sim 1\,\mathrm{nm}^{-1}$ and $\sim 100\,\mu\mathrm{eV}$, respectively. Thus, the expected energy resolution of about $50\,\mu\mathrm{m}$ will undoubtedly contribute to the understanding of the nature of glass-liquid transitions.

1.8 NRS with X-Ray Free Electron Lasers

Impressive achievements and a bright future of NRS studies with synchrotron radiation sources can yet be augmented by emerging opportunities of Nuclear Resonance Scattering with X-Ray Free Electron Lasers (XFELs). In comparison to synchrotrons,

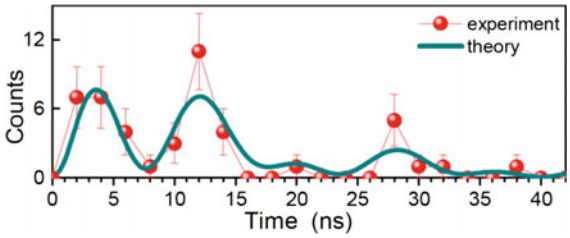

Fig. 1.28 The time evolution of the decay for one (circles) out of twelve registered 50-photon excitations. The solid line is theory fit. The error bars show the standard deviations related to the numbers of counts per channel. (From [111])

these facilities promise to increase the count rate by several orders of magnitude and to allow for NRS pump-probe experiments on the femto-second time scale.

With XFEL radiation, a time spectrum of Nuclear Resonance Scattering can be recorded in a single-shot of a laser pulse. In the first NRS experiment at an XFEL [111], the most probable number of nuclear resonance photons in a single shot was ∼8, the mean number of photons 16, and the maximum number of recorded photons 68. Single-pulse time spectra recorded after a shot with highest photon numbers provide already sufficient statistical accuracy for single-shot hyperfine spectroscopy.

Figure 1.28 shows the time spectrum measured for a single pulse of XFEL radiation with 50 detected photons. The data were fit with the theory using the nuclear magnetic hyperfine splitting as adjustable parameter. The obtained value of the splitting 513(30) neV is in the excellent agreement with the previously reported value of 512.6 neV [135]. The proper determination of the hyperfine parameters is the first demonstration of hyperfine spectroscopy with a single shot of the XFEL radiation.

This result opens access to nuclear resonance pump-probe experiments with femtosecond time resolution at the presently available XFEL facilities and with APD detectors. Indeed, coherent nuclear scattering relies on the phasing of scattering over a nuclear ensemble and occurs only if the phasing/position of atoms are well defined, relative to each other at the excitation and emission time. This condition is valid for solids, but not for liquids. This allows one to use nuclear forward scattering to study, for example, heat transfer or melting (or even magnetic order) on ∼femto-second time scales, only limited by the XFEL pulse length.

Consider the scheme shown in Figure 1.13, where a resonant sample is placed just after the double-crystal monochromator (HHLM). Because the sample is located before high-resolution optics, it is still illuminated by the short pulses of the XFEL, with ∼fs pulse width. Suppose that the sample is melted by a short pulse of a pump laser.

If the sample remains liquid at the arrival of the probe XFEL radiation, the measured spectrum will be the one prepared only by nuclear diffraction in the iron borate crystal. On the contrary, if the sample cools down to a solid state before the arrival of the probe XFEL radiation, the conditions for nuclear forward scattering are fulfilled, and the time spectrum measured after the sample and the iron borate crystal will be

modified. The same approach can be also applied to study dynamics of magnetism by e.g. heating the sample above the Curie point.

1.9 Summary

The article provided a short summary of ideological, instrumental, and scientific developments of Nuclear Resonance Scattering of synchrotron radiation. Comparison of the first pioneering steps in the development of the technique with the gained ability to solve most challenging scientific cases evidences the mature status of this still young field. Moreover, it reveals the permanently increasing rate of the development, opening access to new directions of studies, new types of systems, and new environmental conditions. Thus, there are all reasons to believe in flourishing future of this fascinating way to discover the most intriguing aspects of nature.

Acknowledgements The development of the techniques as well as the waste amount of applications in various scientific fields—only a glimpse could be presented in this article—was only possible with the great involvement of all our colleagues over the years at the beamline and with the users coming to the beamline with incredible ideas for new challenging science. We would as well acknowledge the fruitful collaboration and friendship of our colleagues from the other Nuclear Resonance beamlines at APS, PETRA III, and SPring-8. However, nothing would have started without our mentors, when we were students, E. Gerdau and G. V. Smirnov.

References

1. R.L. Mössbauer, Zeitschrift für Physik **151**(2), 124 (1958). https://doi.org/10.1007/BF01344210
2. R.L. Mössbauer, Naturwissenschaften **45**(22), 538 (1958). https://doi.org/10.1007/BF00632050
3. P.J. Black, P.B. Moon, Nature **188**, 481 (1960)
4. S. Bernstein, E.C. Campbell, Phys. Rev. **132**, 1625 (1963). https://doi.org/10.1103/PhysRev.132.1625
5. P.J. Black, G. Longworth, D.A. O'Connor, Proc. Phys. Soc. **83**(6), 937 (1964). http://stacks.iop.org/0370-1328/83/i=6/a=305
6. G.V. Smirnov, Hyperfine Interactions **27**, 203 (1986)
7. U. van Bürck, Hyperfine Interactions **27**, 219 (1986)
8. E. Gerdau, R. Rüffer, H. Winkler, W. Tolkdorf, C.P. Klages, J.P. Hannon, Phys. Rev. Lett. **54**, 835 (1985)
9. J.P. Hannon, G.T. Trammell, Hyperfine Interactions **123–124**(1–4), 127 (1999). https://doi.org/10.1023/A:1017011621007
10. P. Gütlich, E. Bill, A.X. Trautwein, *Mössbauer Spectroscopy and Transition Metal Chemistry* (Springer, 2011)
11. Yu.V. Shvyd'ko, M. Lerche, J. Jäschke, M. Lucht, E. Gerdau, M. Gerken, H.D. Rüter, H.-C. Wille, P. Becker, E.E. Alp, W. Sturhahn, J. Sutter, T.S. Toellner, Phys. Rev. Lett. **85**, 495 (2000). https://doi.org/10.1103/PhysRevLett.85.495
12. E. Gluskin, E.E. Alp, I. McNulty, W. Sturhahn, J. Sutter, J. Synchrotron Rad. **6**, 1065 (1999)

13. M. Yabashi, K. Tamasaku, T. Ishikawa, Phys. Rev. Lett. **88**, 244801 (2002). https://doi.org/10.1103/PhysRevLett.88.244801
14. Yu.V. Shvyd'ko, M. Lerche, H.-C. Wille, E. Gerdau, M. Lucht, H.D. Rüter, E.E. Alp, R. Khachatryan, Phys. Rev. Lett. **90**, 013904 (2003). https://doi.org/10.1103/PhysRevLett.90.013904
15. R. Röhlsberger, K. Schlage, B. Sahoo, S. Couet, R. Rüffer, Science **328**(5983), 1248 (2010). https://doi.org/10.1126/science.1187770. http://www.sciencemag.org/content/328/5983/1248.abstract
16. E. Gerdau, H. de Waard (eds.), *Nuclear Resonant Scattering of Synchrotron Radiation* (Baltzer Science Publishers, 1999/2000)
17. J.P. Hannon, G.T. Trammell, Phys. Rev. **169**, 315 (1968). https://doi.org/10.1103/PhysRev.169.315
18. J.P. Hannon, G.T. Trammell, Phys. Rev. **186**, 306 (1969). https://doi.org/10.1103/PhysRev.186.306
19. A.M. Afanas'ev, Yu. Kagan, JETP **21**, 215 (1965)
20. A.M. Afanas'ev, Yu. Kagan, JETP **37**, 987 (1973)
21. Yu. Shvyd'ko, *X-Ray Optics—High-Energy-Resolution Applications, Optical Science*, vol. 98 (Springer Publishers, 2004)
22. R. Röhlsberger, Nuclear condensed matter physics with synchrotron radiation, in *Springer Tracts in Modern Physics*, vol. 208 (Springer Publishers, 2004)
23. J.D. Jackson, *Classical Electrodynamics* (Wiley, New York, 1975)
24. H. Wiedemann, *Particle Accelerator Physics I + II* (Springer, Berlin, 1993)
25. T. Tanaka, H. Kitamura, J. Sync. Radiation **16**, 380 (2009). https://doi.org/10.1107/S0909049509009479
26. S.L. Ruby, J. Phys. **35**(C6), 209 (1974)
27. R.L. Mössbauer, Naturwissenschaften **60**, 493 (1973)
28. R.L. Cohen, P.A. Flinn, E. Gerdau, J.P. Hannon, S.L. Ruby, G.T. Trammell, Workshop on new directions in Mössbauer spectroscopy, in *AIP Conference Proceedings*, vol. 38, ed. by G. Perlow (AIP, New York, 1977), pp. 140–148. https://doi.org/10.1063/1.31071
29. E. Gerdau, M. Mueller, H. Winkler, R. Rüffer, European Synchrotron Radiation Facility, in *vol. Supplement I—The Scientific Case*, ed. by Y. Farge, P. Duke (European Science Foundation (ESF), Strasbourg, 1979), pp. 69–75
30. R.V. Pound, G.A. Rebka, Phys. Rev. Lett. **4**, 274 (1960). https://doi.org/10.1103/PhysRevLett.4.274
31. E.P. Team (ed.), *ESRF Foundation Phase Report* (ESRF, Grenoble, 1987)
32. B. Marx, K.S. Schulze, I. Uschmann, T. Kämpfer, R. Lötzsch, O. Wehrhan, W. Wagner, C. Detlefs, T. Roth, J. Härtwig, E. Förster, T. Stöhlker, G.G. Paulus, Phys. Rev. Lett. **110**, 254801 (2013)
33. G.T. Trammell, J.P. Hannon, S.L. Ruby, P. Flinn, R.L. Mössbauer, F. Parak, Workshop on new directions in Mössbauer spectroscopy, in *AIP Conference Proceedings*, vol. 38, ed. by G. Perlow (AIP, New York, 1977), p. 46. https://doi.org/10.1063/1.31071
34. J.P. Hannon, G.T. Trammell, M. Mueller, E. Gerdau, H. Winkler, R. Rüffer, Phys. Rev. Lett. **43**, 636 (1979). https://doi.org/10.1103/PhysRevLett.43.636. URL https://link.aps.org/doi/10.1103/PhysRevLett.43.636
35. J.P. Hannon, N.V. Hung, G.T. Trammell, E. Gerdau, M. Mueller, R. Rüffer, H. Winkler, Phys. Rev. B **32**, 5068 (1985). https://doi.org/10.1103/PhysRevB.32.5068
36. J.P. Hannon, N.V. Hung, G.T. Trammell, E. Gerdau, M. Mueller, R. Rüffer, H. Winkler, Phys. Rev. B **32**, 5081 (1985). https://doi.org/10.1103/PhysRevB.32.5081
37. J.P. Hannon, G.T. Trammell, M. Mueller, E. Gerdau, R. Rüffer, H. Winkler, Phys. Rev. B **32**, 6363 (1985). https://doi.org/10.1103/PhysRevB.32.6363
38. J.P. Hannon, G.T. Trammell, M. Mueller, E. Gerdau, R. Rüffer, H. Winkler, Phys. Rev. B **32**, 6374 (1985). https://doi.org/10.1103/PhysRevB.32.6374
39. R. Röhlsberger, J. Evers, Quantum Optical phenomena in Nuclear Resonant Scattering, in This book, Chapter 3

40. G.T. Trammell, Gamma-ray diffraction by resonant nuclei, in *Chemical Effects of Nuclear Transformations*, vol. I (International Atomic Energy Agency, Vienna, 1961)
41. Yu. Kagan, A.M. Afanas'ev, I.P. Perstnev, JETP **27**, 819 (1968)
42. P.J. Black, I.P. Duerdoth, Proc. Phys. Soc. **84**, 169 (1964)
43. G.V. Smirnov, V.V. Sklyarevskii, R.A. Voskanyan, A.N. Artem'ev, JETP Lett. **9**, 70 (1969)
44. P.P. Kovalenko, V.G. Labushkin, V.V. Rudenko, V.A. Sarkisyan, V.N. Seleznev, JETP Lett. **26**, 85 (1977)
45. R.M. Mirzababaev, G.V. Smirnov, V.V. Sklyarevskii, A.N. Artem'ev, A.N. Izrailenko, A.V. Babkov, Phys. Lett. A **37**, 441 (1971)
46. V.S. Zasimov, R.N. Kuz'min, A.Yu. Aleksandrov, A.I. Firov, JETP Lett. **15**, 277 (1972)
47. A.V. Kolpakov, E.N. Ovchinnikova, R.N. Kuz'min, Phys. Stat. Sol. (b) **93**, 511 (1979)
48. H. Winkler, R. Eisberg, E. Alp, R. Rüffer, E. Gerdau, S. Lauer, A.X. Trautwein, M. Grodzicki, A. Vera, Z. Phys. B **49**, 331 (1983)
49. P.P. Kovalenko, V.G. Labushkin, A.K. Ovsepyan, E.R. Sarkisov, E.V. Smirnov, JETP Lett. **39**, 573 (1984)
50. E. Gerdau, U. van Bürck, R. Rüffer, Hyperfine Interactions **123/124**, 3 (1999)
51. R. Rüffer, Reine Kernbraggstreuung am Yttrium-Eisen-Granat—Eine Methode zur Monochromatisierung von Synchrotronstrahlung. Ph.D. Thesis, Universität Hamburg, Hamburg (1985)
52. T. Mitsui, M. Seto, S. Kikuta, N. Hirao, Y. Ohishi, H. Takei, Y. Kobayashi, S. Kitao, S. Higashitaniguchi, R. Masuda, Japan. J. Appl. Phys. **46**(2R), 821 (2007). http://stacks.iop.org/1347-4065/46/i=2R/a=821
53. W. Sturhahn, E. Gerdau, Phys. Rev. B **49**, 9285 (1994). https://doi.org/10.1103/PhysRevB.49.9285
54. G.V. Smirnov, U. van Bürck, A.I. Chumakov, A.Q.R. Baron, R. Rüffer, Phys. Rev. B **55**(9), 5811 (1997)
55. Q.A. Pankhurst, N.S. Cohen, L.F. Barquín, M.R.J. Gibbs, G.V. Smirnov, J. Non-Cryst. Solids **287**(1–3), 81 (2001). https://doi.org/10.1016/S0022-3093(01)00545-2. http://www.sciencedirect.com/science/article/pii/S0022309301005452
56. T. Mitsui, N. Hirao, Y. Ohishi, R. Masuda, Y. Nakamura, H. Enoki, K. Sakaki, M. Seto, J. Sync. Rad. **16**, 723 (2009)
57. V. Potapkin, A.I. Chumakov, G.V. Smirnov, J.P. Celse, R. Rüffer, C. McCammon, L. Dubrovinsky, J. Sync. Radiation **19**(4), 559 (2012). http://dx.doi.org/10.1107/S0909049512015579
58. G.V. Smirnov, A.I. Chumakov, V.B. Potapkin, R. Rüffer, S.L. Popov, Phys. Rev. A **84**, 053851 (2011). https://doi.org/10.1103/PhysRevA.84.053851
59. M. Seto, R. Masuda, S. Higashitaniguchi, S. Kitao, Y. Kobayashi, C. Inaba, T. Mitsui, Y. Yoda, Phys. Rev. Lett. **102**, 217602 (2009). https://doi.org/10.1103/PhysRevLett.102.217602
60. M. Seto, R. Masuda, M. Saito, Synchrotron-radiation-based energy domain Mössbauer spectroscopy, nuclear resonant inelastic-scattering, and quasi-elastic scattering using Mössbauer gamma rays, in This book, Chapter 2
61. J.B. Hastings, D.P. Siddons, U. van Bürck, R. Hollatz, U. Bergmann, Phys. Rev. Lett. **66**, 770 (1991). https://doi.org/10.1103/PhysRevLett.66.770
62. U. van Bürck, D.P. Siddons, J.B. Hastings, U. Bergmann, R. Hollatz, Phys. Rev. B **46**, 6207 (1992). https://doi.org/10.1103/PhysRevB.46.6207
63. Yu.V. Shvyd'ko, A.I. Chumakov, A.Q.R. Baron, E. Gerdau, R. Rüffer, A. Bernhard, J. Metge, Phys. Rev. B **54**, 14942 (1996). https://doi.org/10.1103/PhysRevB.54.14942
64. D.L. Nagy, L. Bottyán, B. Croonenborghs, L. Deák, B. Degroote, J. Dekoster, H.J. Lauter, V. Lauter-Pasyuk, O. Leupold, M. Major, J. Meersschaut, O. Nikonov, A. Petrenko, R. Rüffer, H. Spiering, E. Szilágyi, Phys. Rev. Lett. **88**, 157202 (2002)
65. A.Q.R. Baron, A.I. Chumakov, R. Rüffer, H. Grünsteudel, H.F. Grünsteudel, O. Leupold, Europhys. Lett. **34**(5), 331 (1996). https://doi.org/10.1209/epl/i1996-00460-0
66. I. Sergueev, U. van Bürck, A.I. Chumakov, T. Asthalter, G.V. Smirnov, H. Franz, R. Rüffer, W. Petry, Phys. Rev. B (Condensed Matter and Materials Physics) **73**(2), 024203 (2006). https://doi.org/10.1103/PhysRevB.73.024203. http://link.aps.org/abstract/PRB/v73/e024203

67. G. Schatz, A. Weidinger, *Nuclear Condensed Matter Physics: Nuclear Methods and Applications* (Wiley, New York, 1996)
68. M. Seto, S. Kitao, Y. Kobayashi, R. Haruki, Y. Yoda, T. Mitsui, T. Ishikawa, Phys. Rev. Lett. **91**, 185505 (2003). https://doi.org/10.1103/PhysRevLett.91.185505
69. A.Q.R. Baron, H. Franz, A. Meyer, R. Rüffer, A.I. Chumakov, E. Burkel, W. Petry, Phys. Rev. Lett. **79**, 2823 (1997)
70. D.C. Champeney, Rep. Prog. Phys. **42**, 1017 (1979)
71. R. Masuda, T. Mitsui, S. Kitao, S. Higashitaniguchi, Y. Yoda, M. Seto, Japan. J. Appl. Phys. **47**(10, Part 1), 8087 (2008). https://doi.org/10.1143/JJAP.47.8087
72. M. Seto, Y. Yoda, S. Kikuta, X.W. Zhang, M. Ando, Phys. Rev. Lett. **74**, 3828 (1995)
73. W. Sturhahn, T.S. Toellner, E.E. Alp, X. Zhang, M. Ando, Y. Yoda, S. Kikuta, M. Seto, C.W. Kimball, B. Dabrowski, Phys. Rev. Lett. **74**, 3832 (1995). https://doi.org/10.1103/PhysRevLett.74.3832
74. A.I. Chumakov, R. Rüffer, H. Grünsteudel, H.F. Grünsteudel, G. Grübel, J. Metge, O. Leupold, H.A. Goodwin, EPL (Europhys. Lett.) **30**(7), 427 (1995). http://stacks.iop.org/0295-5075/30/i=7/a=009
75. A.I. Chumakov, A.Q.R. Baron, R. Rüffer, H. Grünsteudel, H.F. Grünsteudel, A. Meyer, Phys. Rev. Lett. **76**, 4258 (1996). https://doi.org/10.1103/PhysRevLett.76.4258
76. H. Thieß, M. Kaisermayr, B. Sepiol, M. Sladecek, R. Rüffer, G. Vogl, Phys. Rev. B **64**, 104305 (2001)
77. R.A. Brand, Private communication
78. B. Fultz, Private communication
79. R. Röhlsberger, T.S. Toellner, W. Sturhahn, K.W. Quast, E.E. Alp, A. Bernhard, E. Burkel, O. Leupold, E. Gerdau, Phys. Rev. Lett. **84**, 1007 (2000). https://doi.org/10.1103/PhysRevLett.84.1007
80. T. Roth, O. Leupold, H.C. Wille, R. Rüffer, K.W. Quast, R. Röhlsberger, E. Burkel, Phys. Rev. B **71**(14), 140401 (2005). https://doi.org/10.1103/PhysRevB.71.140401
81. R. Callens, R. Coussement, C. L'abbé, S. Nasu, K. Vyvey, T. Yamada, Y. Yoda, J. Odeurs, Phys. Rev. B **65**, 180404 (2002). https://doi.org/10.1103/PhysRevB.65.180404
82. D.P. Siddons, J.B. Hastings, U. Bergmann, F. Sette, M. Krisch, Nuclear Instrum. Methods Phys. Res. Sect. B Beam Interactions Mater. Atoms **103**(3), 371 (1995). https://doi.org/10.1016/0168-583X(95)00654-0. http://www.sciencedirect.com/science/article/pii/0168583X95006540
83. T.S. Toellner, E.E. Alp, W. Sturhahn, T.M. Mooney, X. Zhang, M. Ando, Y. Yoda, S. Kikuta, Appl. Phys. Lett. **67**(14), 1993 (1995). https://doi.org/10.1063/1.114764
84. C. L'abbé, R. Coussement, J. Odeurs, E.E. Alp, W. Sturhahn, T.S. Toellner, C. Johnson, Phys. Rev. B **61**, 4181 (2000). https://doi.org/10.1103/PhysRevB.61.4181
85. R. Röhlsberger, E. Gerdau, R. Rüffer, W. Sturhahn, T. Toellner, A. Chumakov, E. Alp, Nuclear Instrum. Methods Phys. Res. A **394**, 251 (1997)
86. H. Grünsteudel, Nuclear resonant scattering of synchrotron radiation on iron containing biomimetic compounds. Ph.D. Thesis, Medizinische Universiät zu Lübeck, Lübeck (1998)
87. O. Leupold, K. Rupprecht, G. Wortmann, Struct. Chem. **14**, 97 (2003)
88. S. Dattagupta, Phys. Rev. B **14**, 1329 (1976)
89. L. Van Hove, Phys. Rev. **95**, 249 (1954). https://doi.org/10.1103/PhysRev.95.249
90. K.S. Singwi, A. Sjölander, Phys. Rev. **120**, 1093 (1960)
91. V.G. Kohn, A.I. Chumakov, R. Rüffer, Phys. Rev. B **58**, 8437 (1998)
92. W. Sturhahn, V.G. Kohn, Hyperfine Interactions **123/124**, 367 (1999)
93. H.J. Lipkin, Hyperfine Interactions **123/124**, 349 (1999)
94. H.J. Lipkin, Phys. Rev. B **52**(14), 10073 (1995)
95. A.I. Chumakov, G. Monaco, A. Fontana, A. Bosak, R.P. Hermann, D. Bessas, B. Wehinger, W.A. Crichton, M. Krisch, R. Rüffer, G. Baldi, G. Carini Jr., G. Carini, G. D'Angelo, E. Gilioli, G. Tripodo, M. Zanatta, B. Winkler, V. Milman, K. Refson, M.T. Dove, N. Dubrovinskaia, L. Dubrovinsky, R. Keding, Y.Z. Yue, Phys. Rev. Lett. **112**, 025502 (2014). https://doi.org/10.1103/PhysRevLett.112.025502

96. T. Ishikawa, Y. Yoda, K. Izumi, C.K. Suzuki, X.W. Zhang, M. Ando, S. Kikuta, Rev. Sci. Instrum. **63**, 1015 (1992)
97. M. Yabashi, K. Tamasaku, S. Kikuta, T. Ishikawa, Rev. Sci. Instrum. **72**(11), 4080 (2001). https://doi.org/10.1063/1.1406925. http://scitation.aip.org/content/aip/journal/rsi/72/11/10.1063/1.1406925
98. E. Burkel, J. Peisl, B. Dorner, EPL (Europhys. Lett.) **3**(8), 957 (1987). http://stacks.iop.org/0295-5075/3/i=8/a=015
99. I. Sergueev, H.C. Wille, R.P. Hermann, D. Bessas, Yu.V. Shvyd'ko, M. Zając, R. Rüffer, J. Sync. Radiation **18**(5), 802 (2011). https://doi.org/10.1107/S090904951102485X
100. A.I. Chumakov, M.V. Zelepukhin, G.V. Smirnov, U. van Bürck, R. Rüffer, R. Hollatz, H.D. Rüter, E. Gerdau, Phys. Rev. B **41**, 9545 (1990). https://doi.org/10.1103/PhysRevB.41.9545
101. T. Mitsui, M. Seto, R. Masuda, Japan. J. Appl. Phys. **46**(10L), L930 (2007). http://stacks.iop.org/1347-4065/46/i=10L/a=L930
102. T. Mitsui, M. Seto, R. Masuda, K. Kiriyama, Y. Kobayashi, Japan. J. Appl. Phys. **46**(7L), L703 (2007). http://stacks.iop.org/1347-4065/46/i=7L/a=L703
103. T. Mitsui, Y. Imai, R. Masuda, M. Seto, K. Mibu, J. Sync. Radiation **22**(2), 427 (2015). https://doi.org/10.1107/S1600577514028306
104. M. Krisch, A. Freund, G. Marot, L. Zhang, Nuclear Instrum. Methods Phys. Res. Sect. A Accelerators. Detect. Assoc. Equip. **305**(1), 208 (1991). https://doi.org/10.1016/0168-9002(91)90536-Y. http://www.sciencedirect.com/science/article/pii/016890029190536Y
105. R. Barrett, R. Baker, P. Cloetens, Y. Dabin, C. Morawe, H. Suhonen, R. Tucoulou, A. Vivo, L. Zhang, Proc. SPIE **8139**, 813904 (2011). https://doi.org/10.1117/12.894735
106. A. Snigirev, V.G. Kohn, I. Snigireva, B. Lengeler, Nature **384**, 49 (1996)
107. T.M. Mooney, E.E. Alp, W.B. Yun, J. Appl. Phys. **71**(11), 5709 (1992). https://doi.org/10.1063/1.350506
108. O. Hignette, G. Rostaing, P. Cloetens, A. Rommeveaux, W. Ludwig, A.K. Freund, Proc. SPIE **4499**, (2001). https://doi.org/10.1117/12.450227
109. S. Kishimoto, Nuclear Instrum. Methods Phys. Res. A **309**, 603 (1991)
110. A.Q.R. Baron, Hyperfine Interactions **125**, 29 (2000)
111. A.I. Chumakov, A.Q.R. Baron, I. Sergueev, C. Strohm, O. Leupold, Yu. Shvyd'ko, G.V. Smirnov, R. Rüffer, Y. Inubushi, M. Yabashi, K. Tono, T. Kudo, T. Ishikawa, Nature Phys. **14**, 261 (2018). https://doi.org/10.1038/s41567-017-0001-z
112. Multiscalers (2019). https://www.fastcomtec.com/products/ufm/
113. S. Kishimoto, T. Mitsui, R. Haruki, Y. Yoda, T. Taniguchi, S. Shimazaki, M. Ikeno, M. Saito, M. Tanaka, Rev. Sci. Instrum. **85**(11), 113102 (2014). https://doi.org/10.1063/1.4900862
114. P. Fajardo, A.Q.R. Baron, H. Dautet, M. Davies, P. Fischer, P. Göttlicher, H. Graafsma, C. Hervé, R. Rüffer, C. Thil, J. Phys. Conf. Ser. **425**(6), 062005 (2013). http://stacks.iop.org/1742-6596/425/i=6/a=062005
115. S. Stankov, R. Rüffer, M. Sladecek, M. Rennhofer, B. Sepiol, G. Vogl, N. Spiridis, T. Ślęzak, J. Korecki, Rev. Sci. Instrum. **79**(4), 045108 (2008). https://doi.org/10.1063/1.2906321. http://link.aip.org/link/?RSI/79/045108/1
116. I. Kupenko, L. Dubrovinsky, N. Dubrovinskaia, C. McCammon, K. Glazyrin, E. Bykova, T.B. Ballaran, R. Sinmyo, A.I. Chumakov, V. Potapkin, A. Kantor, R. Rüffer, M. Hanfland, W. Crichton, M. Merlini, Rev. Sci. Instrum. **83**(12), 124501 (2012). https://doi.org/10.1063/1.4772458
117. C. Strohm, P. Van der Linden, R. Rüffer, Phys. Rev. Lett. **104**, 087601 (2010). https://doi.org/10.1103/PhysRevLett.104.087601
118. K. Muffler, J.A. Wolny, H.P. Hersleth, K.K. Andersson, K. Achterhold, R. Rüffer, V. Schünemann, J. Phys. Conf. Ser. **217**(1), 012004 (2010). http://stacks.iop.org/1742-6596/217/i=1/a=012004
119. ESRF Upgrade Programme Phase II (2015-2019)—White Paper; ESRF Upgrade Programme Phase II (2015–2022)—Technical Design Study (2013, 2014). www.esrf.eu
120. I. Sergueev, L. Dubrovinsky, M. Ekholm, O.Y. Vekilova, A.I. Chumakov, M. Zając, V. Potapkin, I. Kantor, S. Bornemann, H. Ebert, S.I. Simak, I.A. Abrikosov, R. Rüffer, Phys. Rev. Lett. **111**, 157601 (2013). https://doi.org/10.1103/PhysRevLett.111.157601

121. L. Dubrovinsky, N. Dubrovinskaia, V.B. Prakapenka, A.M. Abakumov, Nature Commun. **3**, 1163 (2012)
122. L. Dubrovinsky, N. Dubrovinskaia, E. Bykova, M. Bykov, V. Prakapenka, C. Prescher, K. Glazyrin, H.P. Liermann, M. Hanfland, M. Ekholm, Q. Feng, L.V. Pourovskii, M.I. Katsnelson, J.M. Wills, I.A. Abrikosov, Nature **525**, 226 (2015)
123. R. Röhlsberger, H. Thomas, K. Schlage, E. Burkel, O. Leupold, R. Rüffer, Phys. Rev. Lett. **89**, 237201 (2002)
124. T.P. Almeida, R. Temple, J. Massey, K. Fallon, D. McGrouther, T. Moore, C.H. Marrows, S. McVitie, Sci. Rep. **7**, 17835 (2017)
125. W. Meissner, R. Ochsenfeld, Naturwissenschaften **21**, 787 (1933). https://doi.org/10.1007/BF01504252
126. I. Troyan, A. Gavriliuk, R. Rüffer, A. Chumakov, A. Mironovich, I. Lyubutin, D. Perekalin, A.P. Drozdov, M.I. Eremets, Science **351**, 1260 (2016)
127. E. Altshuler, T.H. Johansen, Rev. Modern Phys. **76**, 471 (2004)
128. R. Blukis, R. Rüffer, A.I. Chumakov, R.J. Harrison, Meteoritics Planet. Sci. **52**, 925 (2017)
129. J.F.J. Bryson, C.I.O. Nichols, J. Herrero-Albillos, F. Kronast, T. Kasama, H. Alimadad, G. van der Laan, F. Nimmo, R.J. Harrison, Nature **472**, 517 (2015)
130. F. Nestola, V. Cerantola, S. Milani, C. Anzolini, C. McCammon, D. Novella, I. Kupenko, A. Chumakov, R. Rüffer, J.W. Harris, Lithos **265**, 328 (2016)
131. Yu. Shvyd'ko, Phys. Rev. A **91**, 053817 (2015)
132. R. Sinmyo, K. Glazyrin, C. McCammon, I. Kupenko, A. Kantor, V. Potapkin, A.I. Chumakov, R. Rüffer, L. Dubrovinsky, Phys. Earth Planet. Interiors **229**, 16 (2014). https://doi.org/10.1016/j.pepi.2013.12.002. http://www.sciencedirect.com/science/article/pii/S0031920113001921
133. L. Berthier, Physics **4**, 42 (2011)
134. H. Tanaka, T. Kawasaki, H. Shintani, K. Watanabe, Nature Mater. **9**, 324 (2010)
135. U. van Bürck, R.L. Mössbauer, E. Gerdau, R. Rüffer, R. Hollatz, G.V. Smirnov, J.P. Hannon, Phys. Rev. Lett. **59**, 355 (1987)